

Lattice vibrations of the icosahedral solid α -boron

Charles L. Beckel, Mohammad Yousaf,* Mary Z. Fuka, Shagufta Y. Raja, and Ning Lu†

Department of Physics and Astronomy, University of New Mexico, Albuquerque, New Mexico 87131

(Received 27 December 1990)

Crystalline α -boron consists of B_{12} icosahedra in a rhombohedral lattice of $R\bar{3}m$ space-group symmetry. We here carry out a classical force-field analysis of the lattice vibrations. The $\mathbf{q}=\mathbf{0}$ Brillouin-zone vibrations are treated as those of a D_{3d} -point-group-symmetry B_{12} cluster perturbed by intericosahedral crystalline forces; valence-force constants are fitted to account for Raman and ir spectral data. Two-centered intericosahedral bonds are found to be twice as strong as intraicosahedral bonds, while three-centered crystalline bonds are almost as strong as those within a B_{12} unit. The highest-frequency Raman line arises from the breathing mode, strongly perturbed by the two-centered interactions. The lowest-observed-frequency Raman line is attributed to B_{12} libration. As crystal-force-field strengths are turned up, noncrossing of frequencies is encountered; we, therefore, correlate α -crystal modes with I_h regular-icosahedral and D_{3d} B_{12} -cluster modes through eigenvector expansions. Useful classical predictions are made of ir intensities for wave vector $\mathbf{q}=\mathbf{0}$ modes by considering adjacent bond stretching; a prediction of Raman intensities in terms of bond polarizabilities appears to be of very limited value. The phonon analysis is extended from the Brillouin-zone center to the edges by introducing phase-angle differences along two distinct (one C_3 and one C_2) rotational-symmetry axes. The acoustical-branch wave speeds are predicted to be 1.1×10^6 and 0.38×10^6 cm/sec for the c -direction longitudinal and transverse components, respectively. Finally, we consider possible origins of the 525-cm^{-1} Raman line with anomalous polarization and width; most likely this is a Raman electronic line associated with vacancies and B_{11} units.

I. INTRODUCTION

Boron compounds have found extensive use in science and industry. Their possible use as very-high-temperature semiconductors and thermoelectrics has generated renewed interest in the physics and chemistry of boron-rich solids^{1,1a} and is a principal source of motivation for the present work. Here we describe vibrational studies of the simplest crystalline structure for pure elemental boron, α -boron. Although interesting in itself, it also serves as a starting point for the study of vibrations of other, more complicated, icosahedral and rhombohedral boron-rich solids. These include boron carbide, $B_{12}P_2$, $B_{12}As_2$, and $B_{12}O_2$.

The α -boron unit is at the low end in size, mass, and complexity of a wide range of microscopic icosahedral structures that have excited strong interest recently; at the high end, perhaps, is the outer shell of the AIDS virus.² Evidence of 12 atoms positioned at the vertices of a nearly regular icosahedron in crystalline boron carbide was reported almost 50 years ago.^{3,4} A molecule to which I_h symmetry has been ascribed^{5,6} is the borane ion $B_{12}H_{12}^{2-}$, which consists of two concentric regular icosahedra, the inner of boron and the outer of hydrogen atoms. Other observed or proposed icosahedral structures include such diverse entities as the 12 Nb atoms on the 6 faces of an Nb_3Sn $A15$ unit cell,⁷ the Be_{13} component in a UBe_{13} lattice,⁸ Ar_{13} clusters,⁹ icosahedral carborane molecules,¹⁰ dodecahedrane¹¹ ($C_{20}H_{20}$), the icosahedral phase¹² for Al-Si-Mn, a C_{60} truncated-icosahedron molecule with 12 pentagonal and 20 hexago-

nal faces,¹³ the icosahedral form of multiply twinned gold or silver particles,¹⁴ and the shell of a ribonucleic acid containing virus¹⁵ that can cause the common cold in humans. Perhaps icosahedral structures are of special significance because they are closed and multifaced; they offer strength of binding¹⁶ and, for biological systems, protection of vital inner cores.

α -boron is composed of 12-atom icosahedra. The icosahedra are arranged in planes bonded to each other by three-centered bonds within a plane and by two-centered bonds to icosahedra in adjacent planes. The space group is $R\bar{3}m$. Since 6 of the 12 atoms form one type of external bond and the other 6 a different type, an icosahedron is of D_{3d} point-group symmetry rather than regular icosahedral I_h symmetry.

Group-theory properties of α -boron and the relationships of D_{3d} irreducible representations to those of an I_h icosahedron are well understood.¹⁷⁻²⁰ Werheit and Haupt have attempted²¹ a qualitative correlation of α -boron ir spectra with vibrational modes in the free regular B_{12} icosahedron.²² However, description of α - B_{12} phonons across the Brillouin zone has not previously been attempted, and even for the zone center there has been no satisfactory characterization of vibrations in terms of atom-atom interactions.

In the present paper we characterize wave vector $\mathbf{q}=\mathbf{0}$ phonons in terms of a valence-force-field model including intraicosahedral and intericosahedral interactions. We then extend our considerations to phonons with $\mathbf{q}\neq\mathbf{0}$. This work may be considered a major revision and extension of the most thorough previous study of $\mathbf{q}=\mathbf{0}$ pho-

nons, that due to Weber and Thorpe.¹⁷ The Weber and Thorpe (WT) study began with a classical force-field (CFF) description of the $B_{12}H_{12}^{2-}$ molecular ion. To treat α - B_{12} , they removed the 12 H's, added two-centered crystalline interactions to take account of forces between icosahedra in different planes, but found it necessary to set to zero coupling forces between icosahedra in a common lattice plane. They retained unchanged from $B_{12}H_{12}^{2-}$, internal- B_{12} bonds. WT fitted crystalline force constants to the two highest-frequency Raman lines but not to ir data. The Raman spectra¹⁸ they utilized were very reliable in the range of observations, but did not extend below 400 cm^{-1} and included no polarization discrimination. Our $q=0$ results reported here differ markedly from those of Weber and Thorpe. We make use of both Raman *and* ir data; further the Raman data²³ include polarization discrimination. Our analysis considers B_{12} units only, first as an I_h cluster, then a D_{3d} cluster, and finally a D_{3d} unit in an α -crystal. We include three-centered bonds among icosahedra in a common lattice plane and find these to be quite strong. Further, from x-ray-diffraction analysis²⁴ the two-centered bonds linking planes of icosahedra are not radial as in icosahedral boranes. These bonds are distorted 7° from radial in a manner consistent with a significant force by three-centered bonds among icosahedra within a lattice plane. Also, among intericosahedral bonds, only three-centered ones affect ir frequencies and they must be included to fit ir data. Weber and Thorpe considered a very sharp 525-cm^{-1} Raman line to be spurious (which indeed seems to be correct) and dropped it from further consideration. We make some effort to account for this line, either as an ordinary mode of the $q=0$ Raman spectrum or in terms of other possible origins.

In Sec. II we describe the crystal structure and experimental optical spectra of α -boron. Section III contains the details of our normal-mode analyses; there we correlate crystal $q=0$ modes with I_h and D_{3d} cluster modes. In Sec. IV we detail our classical force-field intensity calculations. The extension of results from the center to the edges of Brillouin zones in two distinct directions is given in Sec. V. Finally, in Sec. VI we summarize our findings and highlight unsettled questions.

II. STRUCTURE AND SPECTRA OF α -BORON

A. Crystal structure

α -boron was successfully prepared by McCarty *et al.*²⁵ in 1958. It is stable up to 1200°C and then transforms to a more complicated form, β -boron, at about 1500°C . Decker and Kasper²⁶ studied the crystal structure of the α -boron form by x-ray-diffraction methods. Their results were refined later by Morosin *et al.*²⁴

The basic unit in the α -boron structure is an icosahedron, as shown in Fig. 1, with 12 B atoms at the vertices. A perfect icosahedron, with all its edges of equal length, belongs to the I_h point group. In α -crystalline form, however, the symmetry is lowered to D_{3d} as the edges are not all equal. The polar triangles (1-2-3, and 4-5-6 in Fig. 1) have sides 1.751 \AA each. The equatorial puckered hex-

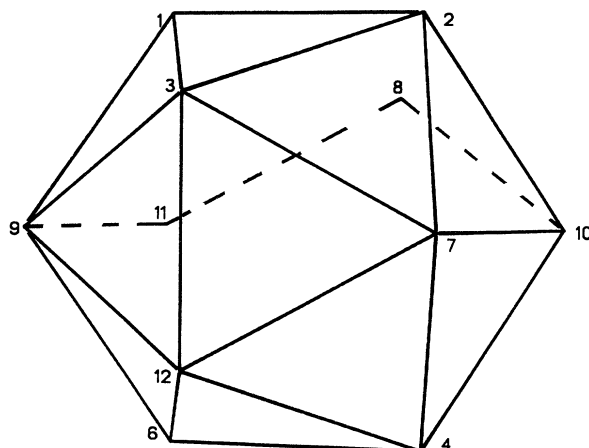


FIG. 1. Numbering of icosahedral atoms. The c or z axis is vertical. Atom No. 5 of the 4-5-6 polar triangle is not shown.

agon (7-10-8-11-9-12) has all sides $=1.782\text{ \AA}$. Each vertex of a polar triangle is connected to three vertices of the equatorial hexagon through two edges of length 1.806 \AA each and one of length 1.801 \AA . We refer to the former (e.g., 3-7 and 3-9 in Fig. 1) as "slant" and the latter (e.g., 3-12) as "vertical," for simplicity.²⁷

The primitive cell is rhombohedral with sides 5.057 \AA and an angle of 58.06° . Visualize one icosahedron at each of the eight rhombohedral vertices in Fig. 2(a). Then a primitive cell consists of the three (north) polar triangle atoms from vertex 1, three (south) polar triangle atoms from vertex 8, and one equatorial atom from each of the other six rhombohedral vertices. (In a hexagonal unit cell description,²⁴ $a_{\text{hex}}=4.927\text{ \AA}$ and $c_{\text{hex}}=12.564\text{ \AA}$.)

The icosahedra lie in planes. Within a plane, icosahedra are bonded to each other by what are called three-centered or Δ bonds, of length 2.019 \AA ; i.e., each hexagon atom forms a three-centered bond with hexagon atoms from two other icosahedra in the same plane. In Fig. 2(b) one such bond is seen (from above) for icosahedra at vertices 2, 3, and 4 of Fig. 2(a). Polar triangle atoms in adjacent-plane icosahedra are connected by ordinary two-centered bonds each of length 1.670 \AA . Seen in Fig. 2(c) is a two-centered link between icosahedra at vertices 1 and 4 of Fig. 2(a). Later, we shall find that the two-centered bonds are stronger than other bonds in the crystal and contribute significantly to the strength in these materials. The intericosahedral three-centered bonds will be shown to be weaker than other bonds in the structure, but still much too strong to be neglected. As mentioned in the Introduction, two-centered bonds are not radially outward from icosahedral centers. They are bent toward the vertical [in Fig. 2(c)] by about 7° . We attribute this to the three-centered bonds which pull icosahedra in a plane closer to each other.²⁸

B. Experimental infrared and Raman spectra

The infrared transmission spectrum of α -boron was reported by Golikova *et al.*²⁹ A total of six bands were

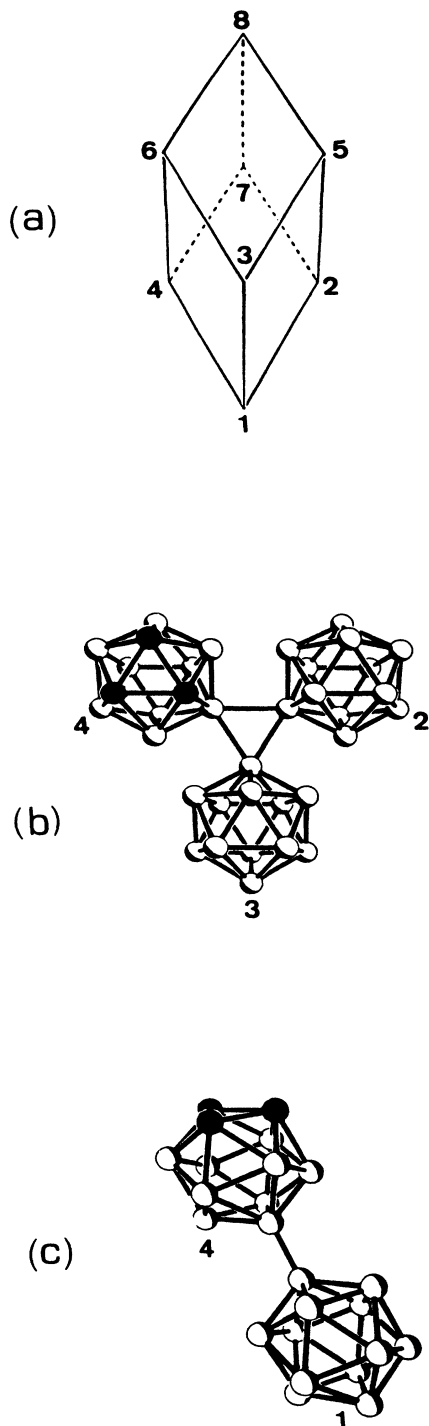


FIG. 2. (a) Numbering of the rhombohedral primitive cell vertices. The c axis is along the 1-8 diagonal. (b) Icosahedra at vertices 2, 3, and 4 as seen looking along the c axis from vertex No. 8 toward No. 1. The three-centered bond linking the icosahedra is shown. Polar triangle atoms Nos. 1, 2, and 3 of icosahedron No. 4 are darkened. (c) The two-centered bond between icosahedra at vertices Nos. 1 and 4. (Special thanks are due R. Schaeffer for help with this figure.)

identified in the range from ~ 400 to 1300 cm^{-1} . Two rather sharp bands at 705 and 806 cm^{-1} were very strong. An absorption centered at 920 cm^{-1} was of intermediate strength, while a feature at 548 cm^{-1} was weak but noticeable. A dip in transmission reported at 1080 cm^{-1} was very broad, while a feature at 1200 cm^{-1} was very weak. Werheit *et al.* obtain comparable results.^{29(a)}

The experimental Raman spectra to which we compare our theoretical frequencies were obtained by Tallant.²³ He observed spectra with resolutions of $\sim 1\text{--}5\text{ cm}^{-1}$ using several different exciting frequencies. Also, using an oriented single crystal, Tallant was able to characterize elements α_{zz} and α_{zx} of the polarizability tensor, thereby discriminating A_{1g} from E_g modes. A spectrum of Tallant's obtained with an exciting line at 6471 \AA is shown in Fig. 3. Note that the Rayleigh scattering at low Raman shift has been subtracted out. This spectrum was made on an unoriented crystal and without polarization analysis. In Table I, column 1, we list Tallant's frequencies, which are considered to be accurate to $\pm 2\text{ cm}^{-1}$. We list Raman frequencies from Refs. 18 and 30 in columns 3 and 5. The three sets of frequencies agree closely. In parentheses are estimated intensities; it should be noted that in different spectra, the intensities can vary appreciably with both exciting frequency and sample orientation. Compare, for example, the intensities for 1186 , 692 , and 175 cm^{-1} in Fig. 3 with corresponding intensities from Ref. 23(a), Fig. 3(c), shown in Table I, column 2. The shoulders at 1198 and 1157 cm^{-1} (also visible but not labeled in the Ref. 30 spectrum) have been described¹⁸ as possibly arising from two-phonon scattering or Fermi resonances. The line at 525 cm^{-1} is present in all known Raman α -spectra, but is far too sharp (width $< 1\text{ cm}^{-1}$) to be accounted for by vibrations in which there is a natural abundance of ^{10}B and ^{11}B . Note that Shelnutt *et al.* label their 524-cm^{-1} line, but not the extremely weak feature at $\sim 710\text{ cm}^{-1}$.

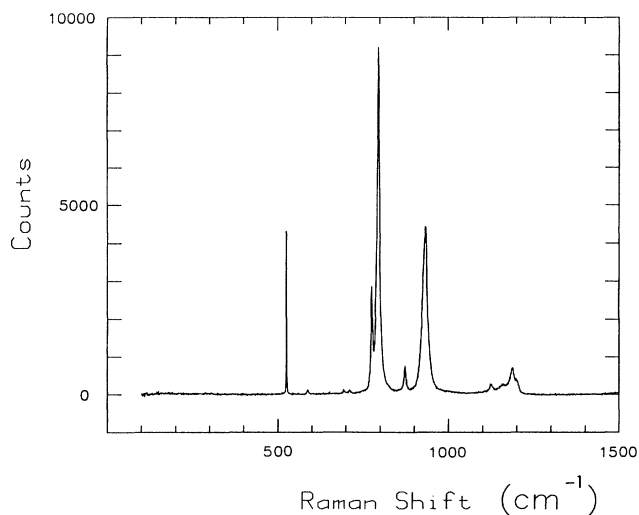


FIG. 3. Raman spectrum for an α -boron crystal obtained by D. Tallant using a 6471-\AA excitation.

TABLE I. Raman frequencies (in cm^{-1}) for α -boron. Intensities relative to the peak at $\sim 795 \text{ cm}^{-1}$ are shown in parentheses.

Tallant <i>et al.</i> ^a	Richter, Weber, and Ploog ^b	Shelnutt <i>et al.</i> ^c
	(1198) (0.05)	
1186 (0.8)	1185 (0.1)	1184 (0.1)
1157 (0.05?)	(1157) (0.02)	
1123 (0.1)	1125 (0.03)	1121 (0.05)
933 (0.7)	931 (0.5)	930 (0.5)
872 (0.03)	872 (0.1)	870 (0.1)
795 (1.0)	796 (1.0)	793 (1.0)
776 (0.2)	776 (0.5)	774 (0.4)
710 (0.01)	710 (0.02)	
692 (0.8)	693 (0.02)	691 (0.1)
587 (0.02)	587 (0.02)	586 (0.02)
525 (0.3)	524 (0.9)	524 (0.4)
175 (0.1)		215 (0.2)

^aReference 23; shifts obtained using a 5145-Å laser excitation.

^bReference 18, with a 6764-Å excitation.

^cReference 30, obtained from a 6328-Å line.

As we shall discuss in the next section, a total of ten single-phonon Raman vibrational lines should be observed, with four of these A_{1g} modes. Tallant has pinpointed the four most intense lines with 5145-Å excitation, 692, 795, 933, and 1186 cm^{-1} , as A_{1g} . However, the 1157- and 1198-cm^{-1} shoulders also have $\alpha_{xz} < \alpha_{zz}$, indicative of A_{1g} . On the other hand, the zz and xz intensities at 525 cm^{-1} are not significantly different, fitting neither the A_{1g} nor E_g assignment. The ten Raman lines with four A_{1g} can be accounted for by ignoring the 1198- and 1157-cm^{-1} shoulders and including two but not three of the lines at 710, 587, and 525 cm^{-1} as E_g modes.

III. VIBRATIONS OF B_{12} CLUSTERS AND $q=0$ MODES OF α -BORON

A. Classification of modes

According to group theory,¹⁷⁻¹⁹ the following types of I_h vibrations will occur for 12 identical atoms at the vertices of a perfect icosahedron:

$$1A_g(1), 1T_{1g}(3), 1G_g(4), 2H_g(5),$$

$$2T_{1u}(3), 1T_{2u}(3), 1G_u(4), 1H_u(5).$$

The prefactor indicates the number that occurs and in parentheses the dimensionality of each listed irreducible representation. The T_{1g} represents a pure rotation and

one T_{1u} a pure translation; thus there are 30 nonzero-vibrational modes with 8 distinct frequencies.

When the symmetry is lowered from I_h to D_{3d} , splitting occurs as is shown in Table II. Twelve identical atoms at the vertices of a D_{3d} icosahedron would have the following representations

$$4A_{1g}, 2A_{2g}, 6E_g, 2A_{1u}, 4A_{2u}, 6E_u.$$

If one subtracts the 6 zero-frequency translational and pure rotational modes, one obtains for a free D_{3d} B_{12} cluster 30 nonzero modes with 20 distinct (barring accidental degeneracy) frequencies in the following representations:

$$4A_{1g}, 1A_{2g}, 5E_g, 2A_{1u}, 3A_{2u}, 5E_u.$$

For a D_{3d} B_{12} primitive cell in a crystal lattice, the pure translations $A_{2u} + E_u$ remain zero-frequency modes ($q=0$), but the rotations $A_{2g} + E_g$ become nonzero-frequency librations. Thus, in α -boron, there will be 22 distinct nonzero frequencies corresponding to 33 independent modes:

$$4A_{1g}, 2A_{2g}, 6E_g, 2A_{1u}, 3A_{2u}, 5E_u.$$

Of these, only ten ($4A_{1g} + 6E_g$) will be Raman active and only eight ($3A_{2u} + 5E_u$) will be infrared active in first order.

TABLE II. Splitting of I_h irreducible representations into D_{3d} modes. The numbers in parentheses indicate dimensionality.

I_h	\rightarrow	D_{3d}	I_h	\rightarrow	D_{3d}
$A_g(1)$	\rightarrow	$A_{1g}(1)$	$T_{1u}(3)$	\rightarrow	$A_{2u}(1) + E_u(2)$
$T_{1g}(3)$	\rightarrow	$A_{2g}(1) + E_g(2)$	$T_{2u}(3)$	\rightarrow	$A_{2u}(1) + E_u(2)$
$G_g(4)$	\rightarrow	$A_{1g}(1) + A_{2g}(1) + E_g(2)$	$G_u(4)$	\rightarrow	$A_{1u}(1) + A_{2u}(1) + E_u(2)$
$H_g(5)$	\rightarrow	$A_{1g}(1) + 2E_g(2)$	$H_u(5)$	\rightarrow	$A_{1u}(1) + 2E_u(2)$

B. Classical models

To determine an accurate quantum mechanical potential surface for a B_{12} unit cell in a lattice with D_{3d} symmetry and 33 degrees of freedom is presently an impossible task. Such potential surfaces can, however, be satisfactorily represented in terms of classical potential contributions. For small oscillations the potential can be represented as a positive definite sum expressed in terms of coordinates representing displacements from an equilibrium configuration. Even if one retains only quadratic and bilinear forms, the number of terms is far too high to permit determination of a unique set of interaction coefficients from 18 experimental frequencies. Fortunately, almost all bilinear terms are extremely small, if one can apply here the results^{31,32} from a Gaussian 86, Hartree-Fock calculation on a $B_{12}H_{12}^{2-}$ molecule. We, thus, adopt a classical valence-force-field (VFF) model³³ for B_{12} . Of course, if the model fails either by not accounting for observed spectra or by yielding nonsensical interaction strengths, we must either use a more complicated model or drop classical modeling altogether. In fact, we find that an even simpler model, with only nearest-neighbor central forces, accounts for most of the observed spectral data in a surprisingly accurate and reasonable way. We believe that this occurs because nearest-neighbor interactions are predominant.

A VFF model has two types of energy terms contributing to total strain energy (TSE) at a given atomic configuration, i.e., to the vibrational potential energy at a point in configuration space. These are

$$V_{ij} = \frac{1}{2} k_{ij} (R_{ij} - R_{ij}^{eq})^2 \quad (1)$$

$$V_{ijk} = \frac{1}{2} A_{ijk} (\theta_{ijk} - \theta_{ijk}^{eq})^2. \quad (2)$$

Here V_{ij} is a Hooke's-law central-force contribution for the interaction between atoms i and j at separation R_{ij} with R_{ij}^{eq} the separation at equilibrium. Equation (2) is a quadratic angular spring interaction term with θ_{ijk}^{eq} the equilibrium angle between bonds ij and jk .

Our computations make use of a scheme originally developed by Boyd³⁴ for determination of equilibrium conformations and normal-mode eigenvectors and frequencies for molecules. For lattice dynamic studies we have made four significant additions/modifications. These introduce (a) crystal forces on unit cells in $\mathbf{q}=\mathbf{0}$ modes, (b) classical infrared and Raman intensity determinations, (c) correlation of vibrational modes in related structures through eigenvector expansions, and (d) determination of $\mathbf{q}\neq\mathbf{0}$ vibrational properties.

C. Cluster modes

α -boron vibrations are perhaps best interpreted as perturbed B_{12} cluster modes; therefore, before discussing lattice phonons, we first describe free B_{12} vibrations. Many α -phonons are intricosahedral modes virtually unaffected by crystalline forces. Other modes, even those strongly altered by intericosahedral forces, can be understood in terms of their cluster origins and specific crystalline perturbations.

In Sec. III C 1 we describe vibrations in a free I_h B_{12} icosahedron. In Sec. III C 2 we detail normal modes for a free D_{3d} B_{12} cluster and correlate D_{3d} and I_h modes. In Sec. III D and III E, respectively, we model α -boron $\mathbf{q}=\mathbf{0}$ lattice modes and correlate these with cluster modes.

1. Regular icosahedron

Regular-icosahedron vibrations were described in Ref. 22. We here summarize I_h -mode visualizations for three reasons: (a) Visualization of I_h vibrations is interesting in itself and has been described only in conference proceedings.²² (b) The geometric distortion from I_h to D_{3d} is actually slight in α -boron. The range of intricosahedral B—B bond lengths²⁴ is 1.751–1.806 Å. (c) Some $\mathbf{q}=\mathbf{0}$ crystal modes retain spectral frequencies and intensities, much as if α -boron was composed of noninteracting icosahedra.

Three symmetry descriptions of an I_h icosahedron are each valuable in understanding individual vibrational modes. In description A (see Fig. 1) a vertical C_3 - S_6 axis passes through the centroids of two polar triangles and one equatorial, six-membered, puckered ring. At equilibrium, the polar triangle atoms 1-2-3 and 4-5-6 are at latitudes 52.62° N and S, respectively, of the circumscribing sphere. The puckered ring atoms are either 10.81° N (atoms 7, 8, and 9) or 10.81° S (10, 11, and 12). Note that the polar triangles are inversions, not projections, of each other. For I_h there are ten C_3 - S_6 axes.

Description B is presented in Fig. 4. Here the vertical line passing through vertices 1 and 4 is a C_5 - S_{10} axis. With 1 and 4 as poles, the two regular planar pentagons are at latitudes 26.57° N and S. The numerical relationship between nearest-neighbor separations R_{B-B} and the radius R of the circumscribing sphere is R_{B-B}

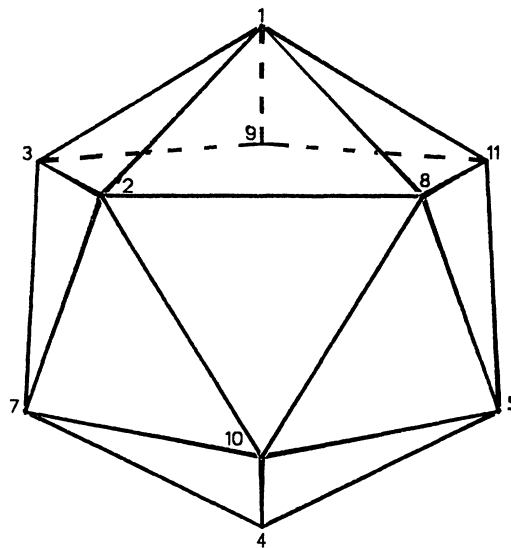


FIG. 4. Icosahedron with five-fold axis vertical, useful for visualizing I_h modes ν_3 , ν_7 , and ν_8 . Atoms Nos. 6 and 12 of the 7-10-5-6-12 pentagon are not shown.

$=1.0515R$. There are six C_5-S_{10} axes connecting opposite vertices.

The third is a cubic description pictured in Fig. 5. Atoms are in pairs on cube faces. Two-centered bonds on opposite faces are parallel while those on adjacent faces are orthogonal. At equilibrium, a vertical C_2 axis bisects bonds 1-2 and 4-6, while these four atoms define a vertical σ symmetry plane. There are 15 distinct C_2 axes and 15 σ planes in I_h . The relationship between R_{B-B} and L , the length of a cube side, is $R_{B-B} = (\sqrt{5}-1)L/2 = 0.618L$ for I_h . In $A15$ Nb_3Sn the Nb atoms are arranged as in Fig. 5; however, on a face $R_{Nb-Nb} = 0.5L$. Thus the 12 Nb atoms on the 6 cube faces form an irregular icosahedron.

To simplify description of I_h oscillations, we incorporate only a central-force Hooke's-law interaction between nearest neighbors. There are 30 such interactions (corresponding to the 30 edges of an icosahedron). Each atom is assigned a mass of 10.8 amu, the mean value using the natural abundance of boron isotopes. Force constants in Eq. (1) are all set to $k_{ij} = 1.3 \times 10^5$ dyn/cm, our optimum value for a VFF model of α -boron; also, we used $R_{ij}^{eq} = 1.77 \text{ \AA}$, the B-B separation in borane molecules.³⁵ Characterization of resulting mode frequency, degeneracy, and type is presented in Table III. We do not use the customary numbering of molecular modes.³³ Rather the ordering is from highest to lowest frequency for clarity in relating I_h eigenmodes to modes after degeneracy splitting.

The ν_1 species is of u symmetry; in each such mode, diametrically opposite atoms have the same displacement in magnitude and direction. The oscillations are best visualized in terms of description A (Fig. 1). The dominant distortion in each ν_1 mode is of a puckered hexagon, the equatorial ring in Fig. 1. About half the strain energy is in the six-ring bonds (rather than 20% for equipartition). Around the ring there is alternation of bond stretch and bond compression at any instant.

The five ν_2 modes can also be interpreted in terms of Fig. 1, but these are of g symmetry. Opposite atoms move in opposite directions, but have the same displacement magnitude at any instant. For each ν_2 mode, $\sim 50\%$ of the total strain energy (TSE) is in the intratriangle and intrahexagon bonds.

Figure 4 is most useful for visualizing the three ν_3 vibrations. For one mode, pentagon 2-3-9-11-8 is contracting (exhalation) at an instant when pentagon 7-12-6-5-10 is expanding (inhalation). At that same instant, polar atom 1 is moving toward the centroid of the contracting

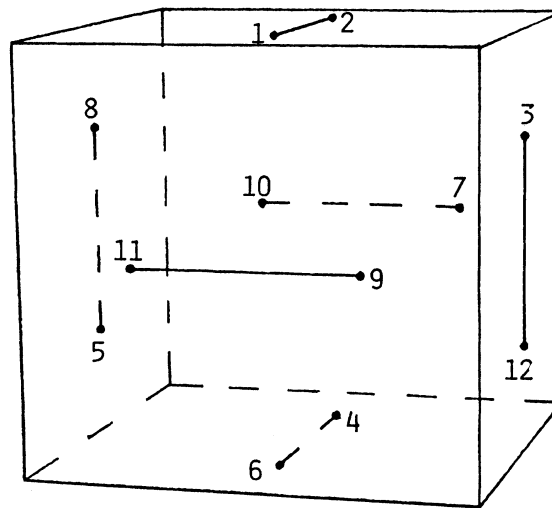


FIG. 5. Cubic description of an icosahedron helpful for I_h modes ν_5 and ν_6 as well as for visualization of $A15$ structure.

pentagon, while polar atom 4 moves away from the centroid of the expanding pentagon. Thus the entire northern hemisphere is contracting, while the southern hemisphere is expanding. Of course, when both polar atoms are heading south, both pentagon centroids must move north to keep the center of mass from displacing.³⁶

The nondegenerate mode ν_4 is pure breathing (dilation) with all atoms moving radially.

All four ν_5 vibrations are similar and can be understood in terms of the cubic description (Fig. 5). Approximately 70% of TSE is due to changes in the six R_{B-B} for the six atom pairs on the cube faces.

The $H_u \nu_6$ modes are perhaps the most difficult to visualize. Four of the five modes involve pairs of opposite tetrahedrons moving almost undistorted on the circumscribing sphere. Three of these four are antisymmetric tetrahedron twists; strain is due to bond-length changes between the eight tetrahedron atoms and the other four atoms. A fourth H_u oscillation involves two tetrahedrons (e.g., 1-3-2-8 and 6-12-4-5 in Fig. 5) sliding on the sphere, without twisting, thereby compressing one bond (5-8) while stretching the opposite bond (3-12); 30% of TSE is in these two bonds. The fifth ν_6 mode is an antisymmetric twist of two pentagons.

The three $T_{2u}(\nu_7)$ oscillations are closely related to those of $T_{1u}(\nu_3)$. The T_{2u} modes also involve antisym-

TABLE III. Normal-mode vibrational degeneracies, symmetries, and frequencies (in cm^{-1}) for a free boron icosahedron that is regular at equilibrium. The mass of each atom is assumed to be 10.8 amu, each spring constant is 1.30×10^5 dyn/cm, and $R_{B-B}^{eq} = 1.77 \text{ \AA}$.

	Deg.	Sym.	Freq.		Deg.	Sym.	Freq.
ν_1	4	G_u	837	ν_5	4	G_g	608
ν_2	5	H_g	835	ν_6	5	H_u	452
ν_3	3	T_{1u}	783	ν_7	3	T_{2u}	395
ν_4	1	A_g	752	ν_8	5	H_g	346

metric pentagon breathing. In ν_7 , however, a polar atom moves toward the centroid of an expanding pentagon, while the opposite polar atom moves away from the contracting pentagon centroid. In T_{2u} the strain energy for bonds between polar and pentagon atoms is one-fourth that in T_{1u} for comparable intrapentagon bond changes.

Visualization is more difficult for the low-frequency $H_g \nu_8$ modes than for those of ν_2 . The ν_8 modes involve pentagon distortions or rocking. More details on these modes can be found in Ref. 22.

2. $D_{3d} B_{12}$ cluster

If one imposes the equilibrium configuration of an α -boron primitive cell on a free B_{12} cluster, the lowering of symmetry splits the I_h modes into those of a D_{3d} icosahedron. We list in Table IV the D_{3d} cluster modes obtained using the same atomic interactions and masses as used for an I_h icosahedron. The splitting due to geometric distortion alone is very small (maximum is 12 cm^{-1} for G_g), and therefore correlation of D_{3d} and I_h modes is unambiguous; the correlation is shown in the I_h -origin columns. We use f_i for D_{3d} cluster frequencies to discriminate from I_h values designated by ν_i . In Table IV we order our f_i from highest to lowest values as we did for frequencies in Table III.

The α -boron vibrational Raman spectrum described in Sec. II B has a wide range of $q=0$ optical-phonon frequencies. The ir spectrum also has, although to a somewhat lesser degree, a wide range of frequencies. The narrower range for a free B_{12} cluster in Table IV indicates that the observed wide ranges must be attributed to strong crystalline forces. This is especially true of two-centered intericosahedral interactions which affect g modes (hence Raman spectra). It also must apply to three-centered forces among icosahedra since the two-centered interactions do not affect u modes (hence ir spectra); without three-centered crystal forces, one might expect to observe only one ir vibrational line from T_{1u} , or two very close lines if resolution were sufficient, since only $I_h T_{1u}$ modes are ir active.

Very brief descriptions for visualizing the individual $D_{3d} B_{12}$ modes are now given.

f_1 . A superposition of $I_h G_u$ modes leads to f_1 . In f_1 the polar triangle 1-2-3 (see Fig. 1) enlarges symmetrically while moving in the $-z$ direction, while triangle 4-5-6 is symmetrically contracting and also moving in the $-z$ direction. While the six triangle atoms move down, the six puckered-hexagon atoms move up to keep the center of mass fixed. All strain energy is in triangle bonds and intertriangle-hexagon bonds.

f_2 . The polar triangles both contract symmetrically while translating away from the icosahedral center of mass in a vertical direction (Fig. 1). About two-thirds of TSE is in the triangle-bond contractions.

f_3 . For these two vibrations, almost 90% of TSE is in the slant and vertical bonds connecting polar triangle and ring atoms.

f_4 . In this pair of modes, 75% of TSE is in triangle atom-ring atom bonds and 20% in polar triangle distortions.

f_5 . This mode retains $I_h G_u$ form. 70% of TSE is in puckered hexagon bonds; around the ring at any instant, there is alternation of stretch and compression.

f_6 . Approximately 40% TSE is in ring hexagon bonds and 40% in the slant bonds. Both f_6 and f_3 are E_g modes originating in the $I_h \nu_2$ vibrations; for f_6 , strain in the ring bonds replaces strain in the vertical bonds in f_3 .

f_7 . The two modes originate in the $I_h T_{1u} \nu_3$ and retain that nature, even though the pentagons involved here are not regular and pole-pentagon equilibrium bond lengths differ. In one hemisphere bonds expand (irregularly), while in the other hemisphere bond lengths shrink. 60% of TSE is in pole-pentagon bonds and 30% in intrapentagon bonds. Looked at from a D_{3d} (Fig. 1) point of view, 97% of TSE is in the slant, hexagon, and vertical bonds.

f_8 . This mode also arises from $I_h T_{1u}$. Here one polar triangle (Fig. 1) is expanding at an instant when the opposite triangle is contracting. Further, all slant bonds connected to the expanding triangle are themselves expanding, while the slant bonds to the contracting triangle are shrinking. Nearly 60% of TSE is in polar triangle bonds and 40% in slant bonds.

f_9 . This arises from the I_h pure breathing mode and remains a breathing mode. Since there are four different equilibrium bond lengths, there is not quite equipartition

TABLE IV. Normal-mode symmetries and frequencies (in cm^{-1}) for a free D_{3d} boron icosahedral cluster. Masses and spring constants are as in Table III, 10.8 amu and $1.3 \times 10^5 \text{ dyn/cm}$, respectively. The equilibrium geometry here is that of an α -boron primitive cell. Presplitting I_h origins are shown.

	Sym.	Freq.	I_h Origin		Sym.	Freq.	I_h Origin
f_1	A_{2u}	844	$G_u(\nu_1)$	f_{11}	A_{1g}	610	$G_g(\nu_5)$
f_2	A_{1g}	837	$H_g(\nu_2)$	f_{12}	A_{2g}	599	$G_g(\nu_5)$
f_3	E_g	836	$H_g(\nu_2)$	f_{13}	E_u	456	$H_u(\nu_6)$
f_4	E_u	835	$G_u(\nu_1)$	f_{14}	A_{1u}	452	$H_u(\nu_6)$
f_5	A_{1u}	834	$G_u(\nu_1)$	f_{15}	E_u	448	$H_u(\nu_6)$
f_6	E_g	834	$H_g(\nu_2)$	f_{16}	A_{2u}	397	$T_{2u}(\nu_7)$
f_7	E_u	784	$T_{1u}(\nu_3)$	f_{17}	E_u	394	$T_{2u}(\nu_7)$
f_8	A_{2u}	781	$T_{1u}(\nu_3)$	f_{18}	E_g	347	$H_g(\nu_8)$
f_9	A_{1g}	752	$A_g(\nu_4)$	f_{19}	E_g	345	$H_g(\nu_8)$
f_{10}	E_g	611	$G_g(\nu_5)$	f_{20}	A_{1g}	344	$H_g(\nu_8)$

of strain energy among bonds.

f_{10} . These are most easily pictured in terms of Fig. 5. For one of the two f_{10} modes, the six cube face bonds 1-2, 3-12, 4-6, 5-8, 7-10, and 9-11 are compressed at any instant when 1-3, 2-10, 4-5, 6-9, 7-12, and 8-11 are stretched. Over 99% of TSE is in these 12 bonds.

f_{11} . The principal movement in this A_{1g} mode is by the three northern hemisphere ring atoms (7,8,9) moving south in Fig. 1 at an instant when the three southern hemisphere atoms (10,11,12) are moving north. Over 60% of TSE is in the slant bonds, which are simultaneously stretching equally.

f_{12} . This is a twist mode. Seen from above in Fig. 1, triangles 1-2-3 and 4-5-6 rotate counterclockwise about the vertical C_3 axis, while the puckered ring rotates clockwise about the same axis. Over 99% of TSE is in the slant bonds, half of which contract, while the other half stretch.

f_{13} . These two are from $I_h \nu_6$ modes and can be pictured in terms of antisymmetric twists of two opposite tetrahedrons. They are better viewed as strains predominantly in the two polar triangles of Fig. 1.

f_{14} . All movement is horizontal in terms of Fig. 1. The predominant motion is an antisymmetric twist without distortion of polar triangles 1-2-3 and 4-5-6. Over two-thirds of TSE is in the slant bonds connecting triangle and hexagon atoms. The rest of TSE is in alternating stretch and compression of hexagon bonds.

f_{15} . The f_{15} have a common I_h origin [$H_u(\nu_6)$] with f_{13} modes. In f_{13} , 50% of TSE is in polar triangle bonds, and in f_{15} , 50% is in vertical bonds (refer to Fig. 1). 30% is in slants and 20% in hexagon bonds in both f_{13} and f_{15} .

f_{16} . In this A_{2u} vibration the six polar triangle atoms move vertically (Fig. 1) in one direction, while the vertical movement of the six hexagon atoms is in the opposite direction. Over 90% of TSE is in the vertical and slant bonds between triangle and hexagon atoms. The hexagon itself distorts significantly, but with very small changes of hexagon bond lengths; the horizontal motion of atoms 7,8,9 is inward when that of 10,11,12 is outward.

f_{17} . The f_{17} retain the nature of the $I_h T_{2u}(\nu_7)$ antisymmetric pentagon breathing modes. However, in D_{3d} , C_5 symmetry is lost and intrapentagon bond lengths are not all equal. Over 50% of TSE is in intrapentagon bond-length changes and over 30% in polar atom-pentagon atom bond-length changes.

f_{18} . These involve hexagon and triangle distortions, the former without, the latter with bond-length changes. 40% of TSE is in triangle, 30% in vertical, and 30% in slant bonds.

f_{19} . Polar triangle atoms vibrate with the largest amplitudes and in directions such that 70% of TSE is in slant bonds.

f_{20} . In this lowest nonzero-frequency mode, the polar triangles 1-2-3 and 4-5-6 in Fig. 1 move in opposite vertical directions, while the puckered hexagon breathes through horizontal atom displacements. The icosahedron oscillates between prolate and oblate configurations. 97% of TSE is in hexagon and vertical bonds.

D. Models applied to α -boron $\mathbf{q}=\mathbf{0}$ modes

1. Simple central-force model

We first applied a simple, three-constant quadratic model with only central forces included. All icosahedral B—B bonds were taken to have the same force constant k_{int} , all external two-centered bonds had k_{2c} , and all external three-centered bonds had k_{3c} . To treat interactions involving links to the 12-atom primitive cell, we introduced image atoms from neighboring cells. Calculated frequencies were fitted only to Raman spectral lines. The predicted ir frequencies could then be compared with experimental values.²⁹ Two types of fits were attempted. In (a) we fitted to nine Raman lines including the one at 525 cm^{-1} but excluding the weak one at 710 cm^{-1} as an experimental line. In (b) we excluded the line at 525 cm^{-1} , but retained the one at 710 cm^{-1} . For both fits (a) and (b), calculated A_{1g} modes were fitted to experimental A_{1g} frequencies. We did not consider the experimental high-frequency shoulders to be $\mathbf{q}=\mathbf{0}$ single-phonon transitions, and we did not include the 175- cm^{-1} line because a libration requires angle-bend interactions.

The results of fitting this model to nine experimental Raman lines are shown at the left of Table V. The force constants both for fits (a) and (b) are shown at the top left. Even though one expects central forces to predominate and all internal interactions to be similar since distortions from I_h are small, still the results for the nine Raman lines are surprisingly reliable. Higher-frequency modes are more accurately fitted than those at lower frequency. This is to be expected since higher frequencies generally are pure stretches, while lower frequencies involve angle bends. The rms errors in the two models are similar and therefore not helpful in choosing between the 525- or 710- cm^{-1} line as a vibrational transition.

At first glimpse, the ir predictions on the right of Table V look bad. However, closer study indicates these results, too, are surprisingly good. The three predicted lines (two low frequency and one intermediate) with no experimental counterparts are found to be weak by methods to be described in Sec. IV. Three of the experimental lines at 920, 705, and 548 cm^{-1} are well predicted in both fits. Both fits (a) and (b) yield almost degenerate modes near 920 cm^{-1} . Each fit yields a reasonably strong line between 705 and 920 cm^{-1} , although the fit to the 806- cm^{-1} line is not too good. Only the 1200- and 1080- cm^{-1} experimental bands are unaccounted for by either fit. In fact, it is difficult to understand how such high-frequency ir lines can arise in α -boron. The two Raman lines above 1000 cm^{-1} are in large part associated with two-centered forces bonding polar triangle atoms in different icosahedra [see Fig. 2(c)]. These are the shortest and almost certainly the strongest bonds in α -boron. However, for u modes, the ir-active ones, these bonds must be rigid. It has been pointed out to us³⁷ that SiO_2 mirror coatings have 1080- and 1200- cm^{-1} absorptions. Indeed, the broad absorbance peak³⁸ at $\sim 1060 \text{ cm}^{-1}$ and the small ripple at $\sim 1200 \text{ cm}^{-1}$ in SiO_2 closely resemble the two high-frequency transmission dips in Fig. 1 of Ref. 29. In the remainder of this paper, we treat the lines at

TABLE V. Simple, three-constant, central-force, quadratic model fitted to α -boron Raman frequencies. Calculated value errors are listed for Raman modes, calculated frequencies for ir lines. Frequencies are in cm^{-1} and force constants in $\text{mdyn}/\text{\AA}$.

Expt	Raman		Infrared		
	Fit (a) $k_{\text{int}}=1.45$ $k_{2c}=2.9$ $k_{3c}=1.0$	Fit (b) $k_{\text{int}}=1.55$ $k_{2c}=2.7$ $k_{3c}=1.0$	Expt	Fit (a)	Fit (b)
1186(A_{1g})	-9	-15	1200		
1123	7	1	1080		
933(A_{1g})	26	46		{ 909	{ 933
			920	{ 908	{ 932
872	2	32		872	902
795(A_{1g})	-39	-28		865	891
776	1	11	806	716	730
710		-39	705	541	556
692(A_{1g})	-54	-33	548	477	493
587	66	-73		422	436
525	-22				
rms error	33	37		31	45

1080 and 1200 cm^{-1} as not being α -boron ir absorption lines. Setting these two and the three weak-intensity lines aside leaves four ir lines to be predicted. The two simple models predict these four unfitted lines just about as well as the nine fitted Raman lines.

Although the two simple three-constant sets in Table V fit the data as well or better than one could have hoped, there remains an ambiguity question. Even when one fits exactly three constants to three frequencies, there are 3! ways of ordering the constants.³⁹ One might question, for example, whether $k_{3c} > k_{2c} > k_{\text{int}}$. This would contradict the generally accepted view that three-centered bonds are weaker than two-centered ones.⁴⁰ Also, k_{int} is close to the intricosahedral $k_{\text{B-B}}$ for central-force and VFF models¹⁷ applied to the borane molecular ion $\text{B}_{12}\text{H}_{12}^{2-}$, where there are no crystal k_{2c} or k_{3c} . Finally, the ordering is consistent with expectations based on bond lengths.

Looking at k values, we see that both models are essentially the same. The two-centered external bonds are about twice as strong as internal bonds. The three-centered external bonds are almost as strong as the intricosahedral ones.

2. Valence-force fields

Before improving on the simple model of the previous section, one should consider the errors to be expected in the better model. If one does not do this, it is easy to fall into a numerology trap. A VFF model can be expected to account for the Raman libration frequency at 175 cm^{-1} and to improve to some extent the prediction of the 710-, 692-, and 587- cm^{-1} Raman lines. But a VFF will not take into account anharmonicities or incorporate bilinear terms other than those introduced by Eq. (2). The leading anharmonic term for the ground state of B_2 introduces a correction to the fundamental vibration⁴¹ of $2\omega_e x_e$ or about 20 cm^{-1} . Thus discrepancies of about 30

cm^{-1} , as found for rms errors in the previous section, are quite reasonable. A closely related question is how many different k_{ij} and A_{ijk} of Eqs. (1) and (2) to incorporate in the VFF model. There are four distinct internal B—B bonds and many distinct internal and external angles in a $\text{B}_{12} D_{3d}$ lattice. We resort to the principle of simplicity. We use as few different interaction constants as account reasonably for experimental results.

In considering incorporation of Eq. (2) interactions, we concerned ourselves with sets of angles, each set to be completely included with a single value of A or to be completely excluded. The sets were the following: 60 internal (to 1 icosahedron) angles each of $\sim 60^\circ$, 60 internal angles each of $\sim 108^\circ$, 30 external angles of $\sim 120^\circ$ (at 2-centered bonds), 6 external angles of 60° (at 3-centered bonds, i.e., 3c), 12 external angles of $\sim 90^\circ$ (3c), 24 external angles of $\sim 108^\circ$ (3c), and 24 external angles of $\sim 143^\circ$ (3c). We incorporated these sets one at a time to find their effects on each normal mode; i.e., we evaluated $\partial\omega/\partial A$, where ω is a predicted α -boron frequency and A an interaction constant. (We had, of course, previously evaluated matrix elements $\partial\omega/\partial k$.) We found that the sets of external 60° , 90° , and 108° had little effect on frequencies. The internal 108° and external 120° sets tended to invert the order of the top two (A_{1g} and E_g) Raman modes. Hence we retained as nonzero contributors to the strain energy only the internal 60° and external 143° sets of 60 and 24 angles, respectively.

In the simple central-force model incorporating either the 525- or 710- cm^{-1} feature as an experimental vibrational line was almost equivalent. We continued to investigate both in VFF model fits. However, we soon found it superior to incorporate the 710- rather than the 525- cm^{-1} line in the sense that we could continue to get improved rms values with the one at 710 but not with that at 525 cm^{-1} . Henceforth, therefore, we will discuss only VFF fits with the 710- cm^{-1} line included and that at 525 cm^{-1} excluded as an α -boron Raman vibrational line. Our best

TABLE VI. Valence-force-field model interaction constants. k 's are in $\text{mdyn}/\text{\AA}$ and A 's in mdyn \AA .

k_{int}	1.3	$A_{60^\circ \text{int}}$	0.15
k_{2c}	3.0	$A_{143^\circ \text{ext}}$	0.15
k_{3c}	1.0	all other A	0

VFF model parameters are listed in Table VI. One should note that there are only five distinct interaction constants.

In Table VII are the calculated vibrations using the VFF model parameters of Table VI. The symmetries and frequency errors of Raman-active and ir-active modes are shown. Also listed are ir modes predicted to be too weak for observation and forbidden-transition modes. All ten Raman-active frequencies are accounted for reasonably; the rms error for these is 23 cm^{-1} , significantly lower than for the nine frequencies of fit (b) in Table V, and the overall rms error for 15 Raman and ir frequencies is 28 cm^{-1} . It seems clear that use of four different k_{int} or more than two different A is not justified in VFF frequency fitting.

The central-force constants in the VFF model retain essentially the same values as in the purely central-force model. The k_{int} is lowered somewhat because of the inclusion of $A_{60^\circ \text{int}}$. It remains true that k_{2c} is about twice as large as k_{int} , while k_{3c} is somewhat smaller than k_{int} , but it is not negligible. Raman frequencies 710, 692, and 587 are better accounted for in VFF, primarily because of $A_{60^\circ \text{int}}$. The librational frequency is fixed by $A_{143^\circ \text{ext}}$.

The strain energies in the VFF model as determined from Eqs. (1) and (2), summed over all interactions of the same type, are indicated in Table VIII; tabulated num-

bers are percentages of TSE for each calculated frequency ω_i . One may note that only four of the α -boron frequencies are significantly affected by two-centered external bonds. No u modes can incorporate $2c$ strain energies since opposite atoms (e.g., 1 and 4) move identically in a u mode and at the Brillouin zone center the image atom of 4 to which 1 is bonded also moves identically. Because of the magnitude of k_{2c} and the large $2c$ contribution to ω_1 and ω_2 modes, these frequencies are much higher than any listed in Table IV for a cluster. Both g and u modes can be affected by three-centered interactions. The lowest-frequencies ω_{21} and ω_{22} correspond to $f=0$ cluster frequencies (free rotations) which were not listed in Table IV; their strains are almost entirely due to angular interactions involving atoms in two different icosahedra.

E. Correlation of $q=0$ crystal modes with D_{3d} cluster modes

1. Eigenvector expansions

The correlation of D_{3d} with I_h cluster modes shown in Table IV is unambiguous because geometric distortion from I_h to D_{3d} is slight in α -boron. On the other hand, correlation of crystal with cluster modes is ambiguous; the two-centered interaction between icosahedra is stronger and the three-centered interaction among icosahedra is almost as strong as intraicosahedral forces. One sees the effects by comparing frequencies of the same species in Tables IV and VIII; for example, the highest A_{1g} frequency in Table VIII is 341 cm^{-1} above the highest A_{1g} in Table IV.⁴²

In Fig. 6 we illustrate for A_g modes how one might try to correlate the α -crystal modes with I_h and D_{3d} cluster modes in a step-by-step process. At the left we show the

TABLE VII. Predicted α -boron $q=0$ modes and frequencies with the valence-force-field interaction constants in Table VI. Symmetries and calculated frequency errors are listed for Raman- and ir-active modes. Also listed are ir-active modes expected to be very weak and inactive modes. All frequencies are in cm^{-1} .

Expt.	Sym.	Calc. value error	Expt.	Sym.	Calc. value error
Raman active					
1186	A_{1g}	-8	776	E_g	24
1123	E_g	26	710	E_g	-17
933	A_{1g}	22	692	A_{1g}	-21
872	E_g	1	587	E_g	-47
795	A_{1g}	-26	175	E_g	-5
Infrared active					
920	A_{2u}	-7	also predicted from the model are ir-active, very weak modes		
	E_u	-11			
806	A_{2u}	58		E_u at 884	
705	A_{2u}	22		E_u at 531	
548	E_u	46		E_u at 449	
Inactive modes					
the model predicts the following inactive modes:					
	A_{2g} at 664			A_{1u} at 883	
	A_{2g} at 180			A_{1u} at 504	

TABLE VIII. Strain energies (%) in VFF model vibrations. The calculated frequencies ω_i are in cm^{-1} . Only contributions of 10% or more are listed.

i	Freq. (ω_i)	Sym.	Δ^a	Hex.	Vert.	Slant	2c	3c	60° int.	143° ext.
(1)	1178	A_{1g}	13			16	61			
(2)	1149	E_g			13	18	62			
(3)	955	A_{1g}	22	18	13			34		
(4)	913	A_{2u}			15	49		24		
(5)	909	E_u		34	23	15		20		
(6)	884	E_u	18			62				
(7)	883	A_{1u}		61		28			10	
(8)	873	E_g	14	31		45				
(9)	864	A_{2u}	53		18			19		
(10)	800	E_g		25		30	16	18		
(11)	769	A_{1g}	24		26		13	21		
(12)	727	A_{2u}	34		29			24		
(13)	693	E_g	19		43				12	
(14)	671	A_{1g}	19	15	10	38			15	
(15)	664	A_{2g}				81			15	
(16)	594	E_u	13		42			11	12	13
(17)	540	E_g	24	18		10		25	11	
(18)	531	E_u	19	18		28			15	
(19)	504	A_{1u}		25		55			17	
(20)	449	E_u	32			46			16	
(21)	180	A_{2g}								93
(22)	170	E_g								81

^a Δ =triangle bonds, Hex=hexagon bonds, vert=vertical bonds, 2c=two-centered external bonds, 3c=three-centered external bonds, 60° int=60° internal angle bends, and 143° ext=143° external angle bends.

four I_h nonzero-frequency g modes that give rise to four A_{1g} and one A_{2g} crystal modes. Along the next vertical axis to the right, the five D_{3d} cluster modes are labeled. Further to the right k_{2c} is increased from 0 to its VFF value of 3.0 $\text{mdyn}/\text{\AA}$ (with $k_{3c}=0$), and finally k_{3c} is turned up (with k_{2c} fixed at 3.0 $\text{mdyn}/\text{\AA}$) from 0 to its final VFF value of 1.0 $\text{mdyn}/\text{\AA}$. The geometry is unchanged as k_{2c} and then k_{3c} are increased. Even though this is a classical, quadratic force-field application, a non-crossing rule applies.⁴³ Two such avoided crossings are seen in Fig. 6 for the four A_{1g} modes. To avoid ambiguity in mode correlation and confusion in the associated interpretation, we resorted to eigenvector expansions.

The 36 normal-mode eigenvectors \mathbf{u}_j for a D_{3d} B_{12} cluster can form a complete orthonormal⁴⁴ set for any 36-dimensional vector. We expanded the α -crystal VFF normalized⁴⁴ eigenvectors \mathbf{v}_i in terms of the D_{3d} cluster set

$$\mathbf{v}_i = \sum_j c_{ij} \mathbf{u}_j. \quad (3)$$

In Table IX we list c_{ij}^2 that are $\geq 10\%$. Because modes from different irreducible representations do not mix, we can conveniently divide this table into four parts. We do not list coefficients for ω_{21} and ω_{22} , which arise from zero-frequency cluster modes.

2. A_g modes

The highest calculated frequency, which we identify with the experimental 1186-cm^{-1} A_{1g} Raman line, arises

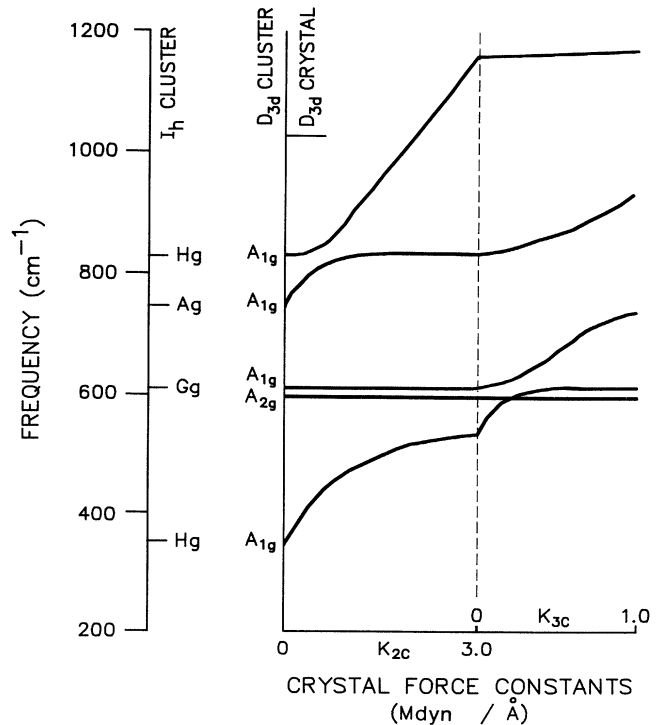


FIG. 6. Correlation of α crystal with B_{12} cluster A_g frequencies. To the left the A_g , G_g , and two H_g frequencies are shown for an I_h cluster. Just to the right are the five A_g frequencies for a D_{3d} cluster. Further to the right, the two types of crystal bonds are turned on.

predominantly from the cluster 752-cm^{-1} breathing mode. It is as if a crossing of the top two curves in Fig. 6 actually took place. Why does the frequency rise so dramatically when crystal forces are included? Radial movement of triangle atoms means double stretch and double compression of the strongest bonds, the two-

centered bonds between icosahedra. Mixing in of f_{20} tends to amplify the vertical movement of triangle atoms while reducing the motion of hexagon atoms; therefore, there is relatively little internal hexagon and external three-centered bond strain. Weber and Thorpe (WT) considered the 1186-cm^{-1} experimental line to be E_g

TABLE IX. Correlation of VFF-calculated α -boron $\mathbf{q}=0$ crystal modes with central-force-field D_{3d} B_{12} cluster modes. Listed are the squares of expansion coefficients c_{ij}^2 (%) that are $\geq 10\%$. Frequencies are in cm^{-1} .

			(a) A_g				
			D_{3d} cluster modes				
			f_2	f_9	f_{11}	f_{12}	f_{20}
			837	752	610	599	344
			A_{1g}	A_{1g}	A_{1g}	A_{2g}	A_{1g}
Crystal modes							
ω_1	1178	A_{1g}		79			18
ω_3	955	A_{1g}	62	14			23
ω_{11}	769	A_{1g}	35				56
ω_{14}	671	A_{1g}			95		
ω_{15}	664	A_{2g}				100	
			(b) E_g				
			D_{3d} cluster modes				
			f_3	f_6	f_{10}	f_{18}	f_{19}
			836	834	611	347	345
			E_g	E_g	E_g	E_g	E_g
Crystal modes							
ω_2	1149	E_g	53				35
ω_8	873	E_g		93			
ω_{10}	800	E_g	32		19	29	19
ω_{13}	693	E_g			66		23
ω_{17}	540	E_g			12	63	21
			(c) A_u				
			D_{3d} cluster modes				
			f_1	f_5	f_8	f_{14}	f_{16}
			844	834	781	452	397
			A_{2u}	A_{1u}	A_{2u}	A_{1u}	A_{2u}
Crystal modes							
ω_4	913	A_{2u}	59		19		22
ω_7	883	A_{1u}		100			
ω_9	864	A_{2u}	41		38		22
ω_{12}	727	A_{2u}			44		56
ω_{19}	504	A_{1u}				100	
			(d) E_u				
			D_{3d} cluster modes				
			f_4	f_7	f_{13}	f_{15}	f_{17}
			835	784	456	448	394
			E_u	E_u	E_u	E_u	E_u
Crystal modes							
ω_5	909	E_u	15	77			
ω_6	884	E_u	80	15			
ω_{16}	594	E_u			10	81	
ω_{18}	531	E_u			85		
ω_{20}	449	E_u					88

arising from a 770-cm^{-1} H_g cluster mode.

The second-highest A_{1g} calculated frequency at 955 cm^{-1} (experimentally 933) has its largest contribution from 837 cm^{-1} A_{1g} and therefore from a $\nu_2 I_h$ origin. Whereas $c_{1,9}$ and $c_{1,20}$ are of opposite sign, $c_{3,9}$ and $c_{3,20}$ are of the same sign. The breathing contributions were in phase for triangle atoms for ω_1 , while the opposite is true for ω_3 . Thus, for ω_3 , it is the three-centered crystal interaction that raises the frequency significantly above that of f_2 ; because the three-centered force constant is only 1.0 mdyn/\AA , the total increase from f_2 is only 118 cm^{-1} . As we do, WT also matched the experimental 933-cm^{-1} Raman line with an A_{1g} theoretical mode. But their theoretical α mode was correlated with the cluster breathing mode.

The experimental A_{1g} mode at 795 cm^{-1} generally is the most intense of the Raman lines. Without the use of graphs or eigenvectors, one would be tempted to correlate this line with the borane molecule B_{12} breathing mode which is observed⁶ at 743 cm^{-1} . However, consideration of radial motion on both two- and three-centered crystal bonds would soon convince one that this correlation must be invalid. We match the 795-cm^{-1} line with the theoretical mode $\omega_{11}=769\text{ cm}^{-1}$, which is a mixture of f_2 (with a high-frequency $I_h H_g$ origin) and f_{20} (from the low-frequency $I_h H_g$). For ω_{11} external three-centered bonds are compressed at an instant when two-centered bonds are stretched, as one expects in the f_{20} oblate configuration. Internally, it is the triangle and vertical bonds that are most strained, as in f_2 . While there is radial motion of hexagon atoms that stresses three-centered external bonds, there is also vertical motion that relieves internal hexagon-hexagon bonds. Because no polarization data were available to them, WT correlated the 795-cm^{-1} experimental lines with a theoretical E_g that arose from the $I_h G_g$ mode.

We match the calculated $\omega_{14}=671\text{ cm}^{-1}$ mode to the experimental 692-cm^{-1} A_{1g} line. This correlates strongly with f_{11} originating from $I_h G_g$. Here, 50 cm^{-1} of the rise in frequency from 610 cm^{-1} is due to the inclusion of 60° internal angle interactions in the VFF model. The mode is almost unaffected by crystalline two- or three-centered forces. Since $I_h G_g$ modes are Raman (as well as ir) forbidden, one might expect the 692-cm^{-1} Raman line to be very weak. It does appear so in Fig. 3. However, in some Raman scattering experiments, e.g., those listed in Table I from Ref. 23, this line is comparatively strong. The experimental 692-cm^{-1} line was matched by WT to an A_{1g} mode with an $I_h H_g$ origin.

The only calculated A_{2g} which does not arise from a pure-rotational cluster mode is ω_{15} . ω_{15} correlates exclusively with the f_{12} mode. Excluding angle bends, the strain for ω_{15} is in internal slant bonds, as for f_{12} . This A_{2g} line (forbidden in both in Raman and ir) was calculated to be at 801 cm^{-1} by WT.

3. E_g modes

There are six $\mathbf{q}=0$, E_g modes in α -boron. According to Tallant, the experimental frequencies are 1123 , 872 , 776 , 710 , 587 , and 175 cm^{-1} . The latter, a librational

mode, arises from zero-frequency rotations; it will be discussed further in Sec. V.

The experimental 1123-cm^{-1} line and theoretical 1149-cm^{-1} line are identified as the same mode. This is a mix of f_3 and f_{19} originating from the high- and low-frequency $I_h H_g$'s, respectively. Much of the ω_2 TSE is in the two-centered bonds connecting icosahedra in different planes, as is the case for the $\omega_1 A_{1g}$. For ω_1 all six external two-centered bonds from one icosahedron are compressed simultaneously. For ω_2 , at a given instant, two of the six may be compressed, two stretched, and two unstrained. The TSE is less for ω_2 than ω_1 for eigenvectors of the same length; the increase in frequency from f_3 to ω_2 is appreciably less than from f_9 to ω_1 . WT associated the 1123-cm^{-1} line with a theoretical A_{1g} mode that arises from a 770-cm^{-1} $I_h H_g$ mode.

ω_8 , which we match with the 872 cm^{-1} experimental Raman line, is the f_6 mode. Over 30 cm^{-1} of the rise from 834 to 873 cm^{-1} is due simply to the inclusion of angle bends in the VFF crystal model. Thus ω_8 is essentially an isolated icosahedron mode. The empirical 872-cm^{-1} line was identified by WT as an E_g mode correlated with a 770 cm^{-1} H_g representation.

The strongest of the E_g lines in Fig. 3 is at 776-cm^{-1} , and we relate this to the calculated $\omega_{10}=800\text{ cm}^{-1}$ mode. The crystal mode has external bonds, both two- and three-centered, strained significantly. Without benefit of polarization discrimination, WT considered the 776-cm^{-1} line to be A_{1g} ; they extrapolated back, on turning off two-centered interactions, to a G_g origin. Using a graph of E_g 's analogous to Fig. 6, we, too, would have traced the 776 cm^{-1} mode to a G_g origin. Table IX(b) shows that ω_{10} is actually a mixture of four of the five contributing cluster modes, based on use of Eq. (3).

The 710-cm^{-1} experimental line we tie to ω_{13} , which is rather strongly correlated with f_{10} . About half of the rise from 611 to 693 cm^{-1} is due to addition of 60° internal angle strains and half to external interactions (each too small to be listed in Table VIII). WT also tie the 710-cm^{-1} line to the fourth-highest calculated E_g frequency, but in their Fig. 3 this correlates with the low-frequency H_g mode.

The lowest observed nonlibrational E_g mode is a weak line at 587 cm^{-1} . Both WT and we tie this to E_g modes that arise from the low-frequency $I_h H_g$ representation. Of the rise from 347 to 540 cm^{-1} , we associate only 30 cm^{-1} with the addition of valence (60° internal angle) forces, the rest to external interactions. Of the external interactions, two-centered ones contribute less than 1% TSE. Three-centered bonds are strained significantly. The distances between one hexagon atom and each of the two bonded external atoms [see Fig. 2(b)] do not change identically; one separation may be increased at an instant when the other is decreased from equilibrium values. WT, with $k_{3c}=0$, probably had significantly strained 108° internal angles.

4. A_u modes

As described in Sec. III D 1 and as is seen in Table VIII, the $\mathbf{q}=0$ ungerade modes cannot incorporate the

strong two-centered external forces; WT, too, calculated in their α -boron model a highest ir-active frequency of 879 contrasted with a highest Raman-active value of 1210 cm^{-1} . We, therefore, do not regard the 1200- and 1080- cm^{-1} lines as true α -boron ir absorptions. However, it should be noted that Werheit and Haupt²¹ (WH) did treat the 1200- and 1080 cm^{-1} lines as ordinary α -boron absorptions and correlated these with $I_h G_u$ and T_{1u} modes, respectively.

After subtracting the 1200- and 1080- cm^{-1} lines, only four observed frequencies remain. Yet group theory predicts that there should be eight ir-active modes. We must account for this difference in terms of degeneracies, low intensities, or lines lying outside the experimental observation range.

The experimentally observed absorption at 920 cm^{-1} we identify with (partially) ω_4 . This mode is a composite of three cluster modes: f_1 , f_8 , and f_{16} . In all three and in ω_4 the internal slant and vertical bonds are strained significantly. The superposition greatly reduces strain in polar triangle bonds. Hexagon atom movements are very much as in f_{16} . The six external interatomic separations involving atoms 7, 8, and 9 (Fig. 1) are stretched equally at an instant when the six external separations from atoms 10, 11, and 12 are compressed equally. These are the three-centered strain forms that raise the ω_4 frequency above those of f_1 , f_8 , or f_{16} . WH correlate this strong experimental line with a G_u origin, which for an I_h system is ir inactive. WT did not publish *ungerade*-mode correlations.

We match the calculated ω_9 mode with the strong ir absorption observed at 806 cm^{-1} . Whereas the combination of f_1 and f_8 canceled much of the internal triangle strain in ω_4 , for ω_9 they add constructively for triangle bonds, but destructively for slant bond strains. The contributions by f_{16} to hexagon atom motion is very much as for ω_4 ; external three-centered bonds from atoms 7, 8, and 9 are stretched equally while those from 10, 11, and 12 are compressed equally. The strong intensity of the 806- cm^{-1} line is due to the strong contribution of f_8 , which arises from the one ir-active I_h mode, i.e., T_{1u} .

On this same basis the 705- cm^{-1} experimental line, which we tie to ω_{12} , should also be strong. This is indeed the case. Superposition of f_8 and f_{16} for ω_{12} leads to strong triangle and vertical but little slant bond internal strains. The hexagon atom movements from f_{16} lead to the same form of three-centered bond contributions to TSE as for the other two A_{2u} modes. WH correlate both the very strong 806- and 705- cm^{-1} observed lines with H_u , an ir-inactive mode for I_h systems.

The other two A_u lines are both ir-inactive A_{1u} 's calculated to be at 883 and at 504 cm^{-1} . These correlate with f_5 and f_{14} , respectively. WT calculated the frequencies for these two to be at 756 and 556 cm^{-1} .

5. E_u modes

There are five E_u modes. Even though there are two avoided E_u frequency crossings as k_{3c} is increased from 0 to 1.0 $\text{mdyn}/\text{\AA}$, the correlations are simpler and clearer

than for the A_{1g} , E_g , or A_{2u} modes. Only one of the five has a strong contribution from f_7 , which correlates with the ir-allowed $I_h T_{1u}$. Thus we might expect only ω_5 to be associated with a strong absorption.

We associate ω_5 as well as ω_4 with the experimental line at 920 cm^{-1} . One would not expect the ir spectrum to have ω_4 and ω_5 resolved. The intraicosahedral distribution of strains in ω_5 is much like that in f_7 . The large hexagonal internal strains and the large external three-centered strains are directly traceable to hexagon atom movements in f_7 .

The ω_6 mode is predominantly f_4 , which originates in $I_h G_u$. In a system with I_h symmetry, the G_u is ir inactive. We find (as described in Sec. IV) ω_6 to be down in intensity from ω_5 by a factor of 30 and thus too weak to be observed. ω_6 has largest icosahedral strains in slant and triangle bond, as one would expect with a strong f_4 contribution. Attributable to f_4 correlation are negligible internal hexagon strains and external three-centered strains of <3% of TSE.

The observed line at 548 cm^{-1} we tie to the $\omega_{16}=594$ cm^{-1} theoretical E_u mode. This arises primarily from the lower E_u mode that originates in the ir-inactive $H_u I_h$ species. One might, therefore, expect ω_{16} to be weak or perhaps unobserved. The 548- cm^{-1} line is indeed weak. Among intraicosahedral bonds the verticals are the most strained as in f_{15} . The relative motion of hexagon atoms is such that internal hexagon strains are negligible, while external three-centered bonds and 143° angle bends are appreciable. WH correlate the 548 cm^{-1} line with $I_h T_{2u}$.

We do not relate $\omega_{18}=531$ cm^{-1} to an observed mode. We determine its intensity to be only about one-fifth that of ω_{16} , and the experimental 548- cm^{-1} line itself is weak. The principal internal strains in ω_{18} are as in f_{13} , although triangle bonds are weaker for ω_{18} . With 3% TSE in external three-centered bonds and 7% in external angle bends, the frequency and strains are altered somewhat from those of an isolated D_{3d} icosahedron.

ω_{20} is also not related to an observed ir line. While we estimate the intensity to be close to that of ω_{16} , this line lies near to the edge of observation. Therefore, we assume that it is likely to be in a region of decreased detection sensitivity. The presence of crystal interactions somewhat perturbs the motion of hexagon atoms from that in f_{17} . About 4% TSE is in external three-centered bonds and angle bends.

One can see from the above discussion how either simple ordering of frequencies or graphical correlation as in Fig. 6 could be misleading. The mode changes with introduction of crystalline forces are comprehensible, but not simple.

IV. CLASSICAL PREDICTION OF INTENSITIES

While frequencies are far more valuable in applying CFF models to spectral data, intensities should not be neglected. With a reasonable level of reliability, intensity models can predict lines not yet recorded that should be observable and can help account for lines that are allowed but are too weak to be observed. Since assignment

of force constants is not unique,³⁹ intensity determinations can reinforce or can cast doubt on assigned interaction strengths.

A B_{12} icosahedron, whether of I_h or D_{3d} symmetry, has no permanent electric dipole moment \mathbf{M} at equilibrium. Further, $\mathbf{M}(R)$ is zero for all nuclear separations R of a B_2 molecule and is very close to zero for individual B—B bonds in α -boron. We must look, therefore, beyond individual bonds for nonzero \mathbf{M} during an oscillation. We seek a procedure that can distinguish two very similar modes, e.g., ν_3 and ν_7 (Table III), by predicting $\mathbf{M} \neq 0$ for one (here ν_3), but $\mathbf{M} = 0$ during the other (ν_7). To be consistent with a classical quadratic potential approximation, the dependence of \mathbf{M} should be linear in atom displacements from equilibrium. Such a procedure can supplement VFF vibrational frequency determinations with classical infrared intensity predictions.

Alben *et al.*,⁴⁵ proposed a method with these characteristics and applied it to homopolar systems, amorphous Si and Ge. We adopt their scheme for a homopolar lattice, i.e., α -boron with its B_{12} primitive cells. The method relies on the assumption that when two adjacent bonds Δ and Δ' undergo different changes in bond length, electron density shifts from one bond, say, Δ , to the other. As a result, a nonzero \mathbf{M} is established, even for homopolars, from the center of Δ' to the center of Δ .

Consider three atoms l , m , and n , with Δ the bond connecting l and m , and Δ' connecting m and n . Let \hat{r}_{ml} be a unit vector from the equilibrium position of m toward the equilibrium position of l . Then $(\hat{r}_{ml} - \hat{r}_{mn})$ is in the direction from the center of Δ' to the center of Δ , assuming Δ and Δ' are of the same length. Call the 3- d displacement from equilibrium of atom l in eigenmode α , $\mathbf{w}_l(\alpha)$. Then the contribution by the adjacent bonds Δ and Δ' due to two different bond-length changes is

$$\mathbf{M}_{m\Delta\Delta'}(\alpha) = (\hat{r}_{ml} - \hat{r}_{mn}) \times [(\mathbf{w}_m - \mathbf{w}_n) \cdot \hat{r}_{mn} - (\mathbf{w}_m - \mathbf{w}_l) \cdot \hat{r}_{ml}]. \quad (4)$$

The total contribution to \mathbf{M} is

$$\mathbf{M}(\alpha) = \sum_m \sum_{\Delta, \Delta'} \mathbf{M}_{m\Delta\Delta'}(\alpha). \quad (5)$$

The m sum is over all atoms in the primitive cell. In a given mode α , we take the predicted intensity to be proportional to $\omega(\alpha)M^2(\alpha)$. In Table X we compare predict-

ed relative ir intensities with experimental values estimated from Fig. 1 of Ref. 29. One notes first that the predicted intensities for forbidden A_{1u} modes $\omega_7 = 883 \text{ cm}^{-1}$ and $\omega_{19} = 504 \text{ cm}^{-1}$ are zero within computer roundoff. (The \mathbf{M} values for all g modes are zero correctly because of cancellation of opposite bond-pair contributions.) The three strongest observed ir lines are also the three strongest predicted lines; however, the $913\text{-}909\text{-cm}^{-1}$ pair are predicted to be too strong and the 864-cm^{-1} mode too weak. In the previous subsection we had already commented on the results for the predicted 884 , 531 , and 449-cm^{-1} modes; the former two may be too weak and the 449-cm^{-1} mode too near the detection limit to be observed.

The experimental values in Table X are estimates from a single source; predicted values incorporate no weighting factors (other than frequency). In light of this, the agreement between experimental and predicted intensities is reasonably good. With regard to weighting of contributions from Eq. (4), we make no *ad hoc* corrections: for different equilibrium angles between Δ and Δ' , for different equilibrium bond lengths, for electron-density distinctions among internal, two-centered, and three-centered external bonds, to take into account permanent atomic charges. That Table X presents a useful comparison is likely because of the nondominant role of density of states and to the near- I_h geometry of the B_{12} units. For boron arsenide, phosphide, and carbide, it will certainly not be possible to neglect atomic charges; atomic movement in an eigenmode will result directly in significant contributions to \mathbf{M} .

In an analogous manner it is possible, in principle, to estimate classically intensities of vibrational Raman lines. Vol'kenshtein^{46,47} proposed treatment of molecular polarizabilities in terms of individual bonds. Long,⁴⁸ using Vol'kenshtein's approximations, formulated a general theory for relative intensities in terms of bond polarizability; Long characterized each bond by three polarizability functions. Alben *et al.*⁴⁵ wrote the three independent forms for each bond in equations analogous to our Eq. (4) above and then summed over bonds and atoms as we do in Eq. (5); they made application to amorphous Si and Ge. Tubino and Piseri⁴⁹ applied the bond polarizability concept to determination of Raman intensities in scattering from covalent crystals, diamond in particular.

We have attempted to apply the bond polarizability concept to prediction of relative Raman intensities in α -boron, but consider the outcome not to be useful. The expressions that we used are closely related to Eqs. (6)–(8) in Ref. 45. Each bond connecting atoms l and m has four contributing factors to $\partial\alpha_{AB}/\partial Q_\epsilon$. Here A and B are space-fixed (i.e., laboratory) Cartesian coordinates and Q_ϵ represents the normal coordinate in eigenmode ϵ . If α_{\parallel} represents the equilibrium polarizability when the electric field \mathbf{E} is parallel to a bond and α_{\perp} the polarizability for \mathbf{E} perpendicular to the bond, then α_{\parallel} , α_{\perp} , $\partial\alpha_{\parallel}/\partial R_{lm}$, and $\partial\alpha_{\perp}/\partial R_{lm}$ all contribute to $\partial\alpha_{AB}/\partial Q_\epsilon$. The former two contribute to the intensity from rotation of the bond in mode ϵ . Tubino and Piseri knew from experiment α_{\parallel} , α_{\perp} , and their derivatives. Such values, to our knowledge, are not available for B—B bonds within or between B_{12}

TABLE X. Comparison of relative intensities for experimental ir and u -mode VFF-predicted lines. Unity is assigned to the strongest mode. Frequencies in cm^{-1} are listed in parentheses.

Expt ^a	Predicted	Expt ^a	Predicted
0.3 (920)	0.6 (913)	1.0 (705)	1.0 (727)
	0.6 (909)	0.1 (548)	0.05 (594)
	0.02 (884)		0.01 (531)
	10^{-6} (883)		10^{-6} (504)
0.8 (806)	0.2 (864)		0.05 (449)

^aEstimated from Fig. 1, Ref. 29.

icosahedra. Thus parametric weighting of independent contributions is necessary. Further, intensities are proportional to the squares of $\partial\alpha_{AB}/\partial Q_\epsilon$, allowing weighting factors with both positive and negative signs. The method does yield the correct forms for the Raman intensities⁵⁰ in terms of laboratory coordinates for each of the D_{3d} irreducible representations. But this alone does not justify publication of results. Because of the high degree of flexibility in choosing parameters to fit experimental intensities, we feel that we cannot present our Raman results as anything more than numerology at this time.

V. BRILLOUIN ZONE AND DISPERSION

In Secs. III and IV we attempted to describe observed optical spectra in terms of $\mathbf{q}=0$ phonons. For a broader understanding of α -boron lattice dynamics, it is necessary to describe vibrations across the Brillouin zone. In this section we consider $\mathbf{q}\neq 0$ vibrations along the two symmetry directions: (a) in the z - or C_3 -axis direction, i.e., along the line connecting vertices 1 and 8 in Fig. 2(a), and (b) in the x - or C_2 -axis direction, i.e., along the line bisecting 9-12 and 8-10 in Fig. 1.

In order to solve the vibrational eigenproblem at a location other than the Brillouin zone center, we introduced as a factor of atomic displacements⁵¹ the quantity $\exp[2\pi i\mathbf{q}\cdot\mathbf{r}(l_1, l_2, l_3)]$. The set of integers (l_1, l_2, l_3) specifies a lattice point. We chose to solve, for each \mathbf{q} , a 72×72 real matrix, whereby each eigenvalue and eigenvector appeared twice.⁵²

A. $q_z\neq 0$

When q_z is increased from 0, with q_x and q_y still 0, the symmetry of the 12-atom unit cell declines from $D_{3d}\rightarrow C_{3v}$. The modes correlate as follows: $A_{1g}\rightarrow A_1$, $A_{2g}\rightarrow A_2$, $E_g\rightarrow E$, $A_{1u}\rightarrow A_2$, $A_{2u}\rightarrow A_1$, and $E_u\rightarrow E$ (see Appendix IV of Ref. 53). Thus mode degeneracy is retained, but g and u symmetry are lost.

A plot of the dispersion curves ω versus q_z for the 36 modes (24 frequencies) is shown in Fig. 7. Two characteristics most obvious are the complexity and the near-zero slope of most curves. Labeling is avoided because of the large number of modes; however, the symmetries at the Γ point ($q_z=0$), and therefore at any q_z , can readily be determined from columns 2 and 3 of Table VIII. Loss of g and u symmetry is seen in the avoided crossing at about $q_z=0.04\text{ \AA}^{-1}$ of two modes, one of which was A_{2u} (727 cm^{-1}) and the other A_{1g} (671 cm^{-1}) at the Γ point. At $q_z=0.04\text{ \AA}^{-1}$ both are of the same A_1 symmetry and therefore "repel."

The edge of the zone in Fig. 7 corresponds to a phase difference of π between adjacent constant- z planes containing lattice points in Fig. 2(a). For greater phase differences, each dispersion curve folds back on itself. At the zone edge, lattice points 1 and 5,6,7 are all in phase; points 2,3,4 and 8 are in phase with each other, but π out of phase with the former four. This occurs when $2\pi q_z c_{\text{hex}}=3\pi$ or $q_z=1.5/12.56=0.119\text{ \AA}^{-1}$. When $q_z=0.119\text{ \AA}^{-1}$, the symmetry reverts to D_{3d} . However, here a primitive cell is composed of 24 rather than of 12

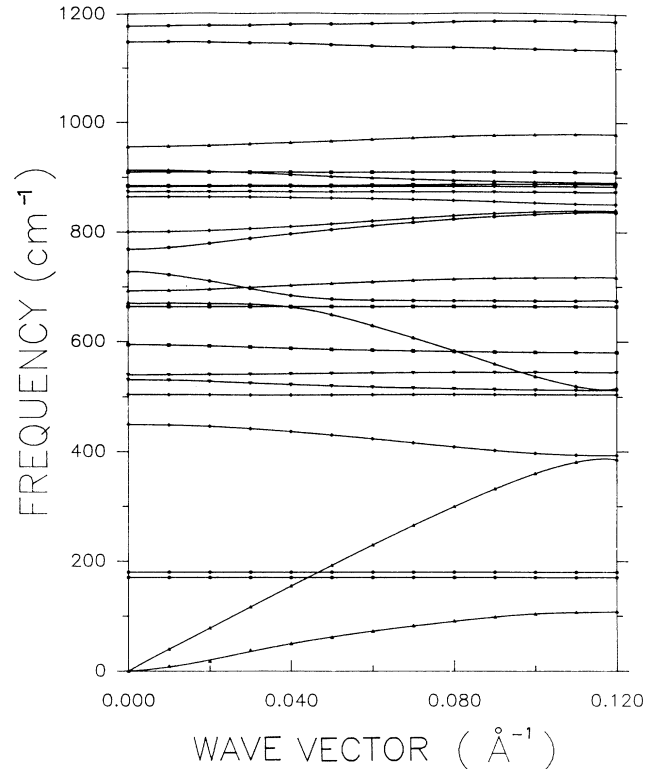


FIG. 7. α -boron dispersion curves obtained with phase difference in the c direction.

atoms. At $q_z=0$ an inversion center during a normal-mode oscillation can be at the midpoint of the long diagonal in Fig. 2(a), the midpoint of the two-centered bond in Fig. 2(c), or at the center of any icosahedron. Such points are not all equivalent at the q_z -zone edge; symmetry operations with the midpoint of the two-centered bond fixed would yield that the highest-frequency mode is A_{1g} ; inversion through an icosahedron center yields A_{2u} . This mode is not an icosahedral breathing mode, but does stretch two-centered bonds. Hence it has the highest frequency at $q_z=0.119\text{ \AA}^{-1}$.

The three Γ -point translational modes split into a TA (two-fold) mode which rises to 108 cm^{-1} and an LA (one-fold) mode with $\omega=389\text{ cm}^{-1}$ at the edge. (The apparent initial positive curvature for the TA mode is not real, but an artifact of our frequency-determining and plotting imprecision.) If we least-squares fit straight lines to the two lowest curves in Fig. 7 with $q_z\leq 0.05\text{ \AA}^{-1}$, we obtain for the acoustic-branch phase velocities $c_z(\text{LA})=1.1\times 10^6\text{ cm/sec}$ and $c_z(\text{TA})=0.38\times 10^6\text{ cm/sec}$.

B. $q_x\neq 0$

The dispersion curves obtained on increasing q_x are shown in Fig. 8. The x axis is in an \mathbf{a}_{hex} direction and a full range of ω values for each curve is obtained between $q_x=0$ and $1/a_{\text{hex}}=0.203\text{ \AA}^{-1}$. The symmetry changes from D_{3d} at the Γ point through C_2 to C_{2h} at the right-hand edge. In general, excluding $q_x=0$, there are 36 non-

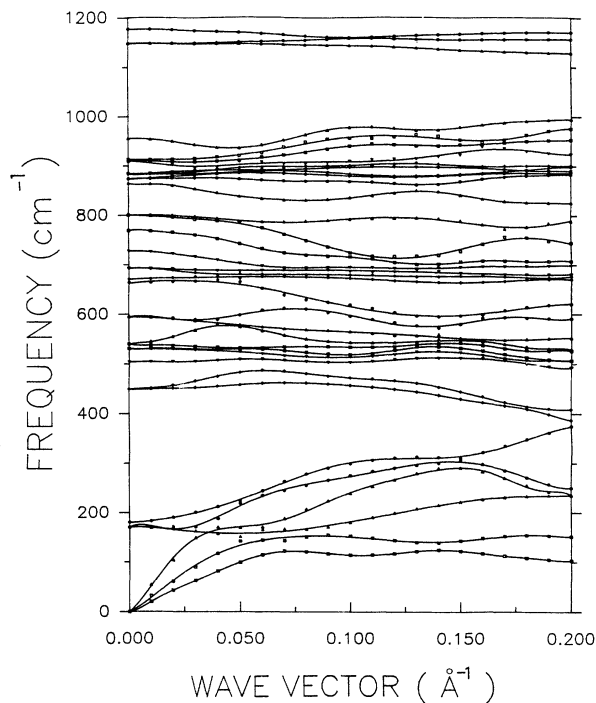


FIG. 8. Dispersion curves when $q_x \neq 0$ (but $q_y = 0 = q_z$). The x direction is from vertex No. 4 to No. 2 in Fig. 2(a).

degenerate modes. Only at the zone center and zone edge is g or u symmetry present. At the zone edge the phase difference is 2π between one icosahedron and either of the two nearest neighbors displaced only in the x direction from the one in question; it is π from that icosahedron to each other nearest-neighbor icosahedron in the same constant- z plane.

As q_x increases from zero, the irreducible representations correlate⁵³ as follows: $A_{1g} \rightarrow A$, $A_{2g} \rightarrow B$, $E_g \rightarrow A + B$, $A_{1u} \rightarrow A$, $A_{2u} \rightarrow B$, and $E_u \rightarrow A + B$; at the edge $A \rightarrow A_g$ or A_u , $B \rightarrow B_g$ or B_u . Thus, as q_x increases from 0 to 0.203 \AA^{-1} , the 1178-cm^{-1} A_{1g} mode becomes an A , crosses a B , and finally becomes an A_g mode with $\omega = 1157 \text{ cm}^{-1}$. The 1149-cm^{-1} E_g mode splits into a B and A which become B_u at 1171 cm^{-1} and A_u at 1129 cm^{-1} at the edge. All retain strongly strained two-centered bonds.

One may note that the slopes need not be zero at the edge where the symmetry is C_{2h} . Further, there are no vibrations at any q_x in the $1000\text{--}1100\text{-cm}^{-1}$ range. This was also true for $q_z \neq 0$. On the other hand, crowding and mixing of modes is great at $\sim 900 \text{ cm}^{-1}$.

Since there is no degeneracy, there are three acoustic modes. The highest of the three is an A mode and corresponds at low q_x to an icosahedral translation in the x direction, i.e., is longitudinal; the phase velocity near the Γ point is $1.5 \times 10^6 \text{ cm/sec}$. The middle acoustic mode has B symmetry, corresponds to transverse motion in the y direction (i.e., perpendicular to the c axis), and has phase velocity at low q_x of $0.9 \times 10^6 \text{ cm/sec}$. The lowest vibration also is B and corresponds to translations in the z direction with phase velocity $0.7 \times 10^6 \text{ cm/sec}$.

C. Comparison with experiment

Unfortunately, we know of no experiments on α -boron directly comparable to our Brillouin-zone predictions. Gieske, Aselage, and Emin⁵⁴ have measured acoustic velocities in boron carbides. For 20 at. % carbon the longitudinal velocity is 1.4×10^6 and for 10 at. % is $1.2 \times 10^6 \text{ cm/sec}$. The transverse velocities are 0.9 and 0.75 cm/sec , respectively, for the two distinct carbon concentrations. These experimental measurements are averages over all directions and elastic constants. In so far as comparison is possible, the agreement of our predictions with the low carbon experimental values is acceptable. When better predictions are required, it will be necessary to take into account VFF model limitations.⁵⁵

VI. CONCLUDING REMARKS

As described in earlier sections, a classical valence-force field accounts quite well for observed Raman and infrared spectral characteristics. The model also helps one understand structure, bonding, lattice dynamics, and related characteristics of α -boron.

Among questions raised but unanswered in the paper, one stands out for its potential importance. This concerns the sharp, intense, "spurious," Raman line at 525 cm^{-1} . The line is anomalously sharp for elemental boron with a natural isotopic mix, shows anomalous polarization, and is present with use of a variety of different instruments and exciting frequencies^{18,23,30} in all samples used. It does not appear in the infrared.²⁹ Possible causes include the following.

(a) Accidental degeneracy of an A_{1g} and an E_g mode to account for the anomalous polarization. But this would lead to too many observed Raman modes and the composite line would still have a width characteristic of a natural abundance.

(b) A bulk impurity such as Cl_2 or Si. Chlorine is often present during α preparation and as interstitial Cl_2 might have a vibration in the 530-cm^{-1} range. However, Cl is sometimes not present during preparation and itself has significant isotopic mixing. Si has a sharp 523-cm^{-1} line, but α samples would all have to have heavy Si concentration formed into large tetrahedrally bonded Si clusters.

(c) Surface contaminants or surface structure distinct from bulk. But the 525-cm^{-1} shift is far too intense to have a surface origin.

(d) The line is due to a multiphonon process. But this would require large groups of B atoms (24 or 36 is insufficient) acting as a vibrational unit with a very high density of states.

(e) The line is associated with an electron transition. But a perfect α -boron crystal has a 2-eV gap.⁵⁶ None of the above explanations accounts satisfactorily for the anomalous Raman shift.

Suppose, however, that a defect arises naturally in boron during preparation of the α form, that occurs in the bulk, and that results in two electronic states between which Raman transitions are allowed but ir transitions are forbidden. The two vibrational surfaces would have to be very similar in form near the potential minima or

else zero-point energy differences would be isotope dependent.

We further note that there are two stable forms of B_{11} cages known among borane molecules.⁵⁷ One is a truncated icosahedron, open, and with only 11 vertices; the other is a closed octadecahedron. The latter is presumed to be the lower energy form. If during α -boron growth a B_{11} cage forms and closes before a 12th atom can be added, a vacancy defect is created. The local structure will be altered as will the electronic states as a result of the defect.

We therefore propose that the 525-cm^{-1} shift arises from a Raman transition between two electronic states separated in their ground vibrational states by 0.0650 eV . Electronic Raman spectra are well known.^{58,59} It is even possible that very shallow electronic levels were observed long ago for α -boron.⁶⁰

We were led to consider defects simply to account for a

spurious Raman shift. The effect, however, of such defects on structure, mechanical characteristics, electron transport, entropy, and other thermodynamic properties could be quite significant. Also, B_{11} cages might not be confined to α -boron. Similar vacancy defects could occur in other icosahedral and rhombohedral boron solids.

ACKNOWLEDGMENTS

This work was supported by U.S. Department of Energy Grant No. DE-FG04-86ER45272, Jet Propulsion Laboratory Contract No. 957760, and Sandia National Laboratories Contract Nos. 06-7585 and 75-3965. The authors are especially grateful to David Tallant for providing Fig. 3 and many unpublished, useful pieces of information. They further acknowledge very useful conversations with or other help from Terry Aselage, Bruno Morosin, David Emin, Peter Lax, Riley Schaeffer, and John Shelnett.

*Permanent address: Electronics Division, PINSTECH, Islamabad, Pakistan.

† Present address: Program Development Corporation, 300 Hamilton Ave. White Plains, N.Y. 10601.

¹*Boron-Rich Solids*, (University of New Mexico, Albuquerque, New Mexico), Proceedings of an International Conference on the Physics and Chemistry of Boron and Boron-Rich Borides, AIP Conf. Proc. No. 140, edited by D. Emin, T. Aselage, C. L. Beckel, I. A. Howard, and C. Wood (AIP, New York, 1986).

^{1a}*Boron-Rich Solids, 1990*, Proceedings of the 10th International Symposium on Boron, Borides and Related Compounds (Albuquerque, New Mexico), AIP Conf. Proc. No. 231, edited by D. Emin, T. Aselage, C. L. Beckel, A. C. Switendick, and B. Morosin (AIP, New York, in press).

²M. Koch, *New Sci.*, 26 March 1987, p. 46.

³G. S. Zhdanov and N. G. Sevast'yanov, *Dokl. Akad. Nauk SSSR C.R.* **32**, 432 (1941).

⁴H. K. Clark and J. L. Hoard, *J. Am. Chem. Soc.* **65**, 2115 (1943).

⁵J. Wunderlich and W. N. Lipscomb, *J. Am. Chem. Soc.* **82**, 4427 (1960).

⁶E. L. Muettterties, R. E. Merrifield, H. C. Miller, W. H. Knoth, Jr., and J. R. Downing, *J. Am. Chem. Soc.* **84**, 2506 (1962).

⁷L. R. Testardi, *Rev. Mod. Phys.* **47**, 637 (1975).

⁸A. I. Goldman, S. M. Shapiro, D. E. Cox, J. L. Smith, and Z. Fisk, *Phys. Rev. B* **32**, 6042 (1985).

⁹J. Farges, M. F. de Feraudy, B. Raoult, and G. Torchet, *J. Chem. Phys.* **78**, 5067 (1983); J. Jellinek, T. L. Beck, and R. S. Berry, *ibid.* **84**, 2783 (1986).

¹⁰R. N. Grimes, *Carboranes* (Academic, New York, 1970).

¹¹R. J. Ternansky, D. W. Balogh, and L. A. Paquette, *J. Am. Chem. Soc.* **104**, 4503 (1982); L. A. Paquette, P. J. Ternansky, D. W. Balogh, and G. Kentgen, *ibid.* **105**, 5446 (1983).

¹²See, e.g., P. J. Steinhardt, *Science* **238**, 1242 (1987) or M. La Breque, *Mosaic* **18**, No. 4, pp. 2-23 (National Science Foundation, Wash., D.C.) Winter 1987/1988.

¹³H. W. Kroto, J. R. Heath, S. C. O'Brien, R. F. Curl, and R. E. Smalley, *Nature* **318**, 162 (1985). Very recently, solid C_{60} has been reported by W. Krätschmer *et al.*, *Nature* **347**, 354 (1990).

¹⁴L. D. Marks and D. J. Smith, *J. Cryst. Growth* **54**, 425 (1981); D. J. Smith and L. D. Marks, *ibid.* **54**, 433 (1981).

¹⁵M. G. Rossman, E. Arnold, J. W. Erickson, E. A. Frankenburg, J. P. Griffith, H.-J. Hecht, J. E. Johnson, G. Kamer, M. Luo, A. G. Mosser, R. R. Rueckert, B. Sherry, and G. Vriend, *Nature* **317**, 145 (1985).

¹⁶It was pointed out by F. C. Frank [*Proc. R. Soc. London A* **215**, 43 (1952)] that a group of 12 argon atoms in contact with a 13th central Ar is more strongly bound by Lennard-Jones forces when in a regular icosahedron rather than in either a face-centered-cubic or hexagonal-close-packed arrangement. A. J. Stone [*Inorg. Chem.* **20**, 563 (1981)] generalized the argument for maximum binding energy in terms of Euler's formula for a convex polyhedron $n_V + n_F = n_E + 2$, where n_V is the number of vertices, n_F is the number of faces, and n_E is the number of edges; for a given number of atoms (vertices), triangular faces maximize the number of edges; i.e., the number of two-centered bonds. Note, if the faces are all triangular, this also maximizes the number of face bonds, i.e., three-centered bonds. An icosahedron is in a sense an optimum triangular-faced structure.

¹⁷W. Weber and M. F. Thorpe, *J. Phys. Chem. Solids* **36**, 967 (1975).

¹⁸W. Richter, W. Weber, and K. Ploog, *J. Less-Common Met.* **47**, 85 (1976).

¹⁹H. Binnenbruck and H. Werheit, *Z. Naturforsch. A* **34**, 787 (1979).

²⁰For recent reviews on the vibrations of α -boron and related materials, see H. Werheit, *Boron-Rich Solids* (Ref. 1) p. 325, or H. Werheit, in *Proceedings of the 9th International Symposium on Boron, Borides and Related Compounds*, edited by H. Werheit (University of Duisburg, Duisburg, FRG, 1987), p. 142.

²¹H. Werheit and H. Haupt, *Z. Naturforsch. A* **42**, 925 (1987).

²²C. L. Beckel and J. P. Vaughan, in *Boron-Rich Solids* (Ref. 1) p. 305.

²³(a) D. R. Tallant, T. L. Aselage, A. N. Campbell, and D. Emin, *Phys. Rev. B* **40**, 5649 (1989); (b) D. R. Tallant (unpublished).

²⁴B. Morosin, A. W. Mullendore, D. Emin, and G. A. Slack, in *Boron-Rich Solids* (Ref. 1) p. 70, and references cited therein.

- ²⁵L. V. McCarty, J. S. Kasper, F. H. Horn, B. F. Decker, and A. E. Newkirk, *J. Am. Chem. Soc.* **80**, 2592 (1958).
- ²⁶B. F. Decker and J. S. Kasper, *Acta Crystallogr.* **12**, 503 (1959).
- ²⁷Slant and vertical refer to directions of bond projections on a vertical plane (e.g., passing through atoms 7 and 9 in Fig. 1).
- ²⁸A very rough analogy to boron flexibility in two- or three-atom binding might be drawn to two-quark (meson) or three-quark (baryon) binding.
- ²⁹O. A. Golikova, J. A. Drabkin, V. K. Zaitsev, M. M. Kazanin, D. N. Mirlin, J. V. Nelvson, E. Tkalenko, and T. Chomidov, in *Proceedings of the International Symposium on Boron*, Tbilisi, 1972 (Mecniereba, U.S.S.R., 1974), pp. 44-58.
- ^{29a}H. Werheit, U. Kuhlmann, N. E. Solov'ev, G. P. Tsiskarishvili, and G. Tsagareishvili, in *Boron-Rich Solids, 1990* (Ref. 1a).
- ³⁰J. A. Shelnutt, B. Morosin, D. Emin, A. Mullendore, G. Slack, and C. Wood, in *Boron-Rich Solids* (Ref. 1), p. 312.
- ³¹T. A. Green, A. C. Switendick, and D. Emin, *J. Chem. Phys.* **89**, 6815 (1988).
- ³²T. A. Green (unpublished).
- ³³G. Herzberg, *Infrared and Raman Spectra of Polyatomic Molecules* (Van Nostrand, Princeton, 1945).
- ³⁴R. H. Boyd, *J. Chem. Phys.* **49**, 2574 (1968).
- ³⁵W. N. Lipscomb, *Boron Hydrides* (Benjamin, New York, 1963).
- ³⁶The simultaneous displacements of all 12 atoms can be determined in terms of the Legendre polynomial $P_1(\cos\theta)$.
- ³⁷H. J. Stein (private communication).
- ³⁸A. S. Tenney and J. Wong, *J. Chem. Phys.* **56**, 5516 (1972); see top of Fig. 1.
- ³⁹C. D. Needham and J. Overend, *Spectrochim. Acta* **22**, 1383 (1966).
- ⁴⁰See, e.g., harmonic force constants for diborane: J. L. Duncan, J. Harper, and E. Hamilton, *J. Mol. Spectrosc.* **102**, 416 (1983).
- ⁴¹K. P. Huber and G. Herzberg, *Constants of Diatomic Molecules* (van Nostrand Reinhold, New York, 1979).
- ⁴²Only 2 cm^{-1} of the 341-cm^{-1} rise is attributable to 60° internal angle bends included for Table VIII but not for Table IV frequencies.
- ⁴³V. I. Arnold, *Mathematical Methods of Classical Mechanics* (Springer-Verlag, New York, 1978), Appendix 10.
- ⁴⁴Eigenvectors are normalized in angstroms for the expansions, but not for calculations of frequencies or strain energies; that would violate the small-amplitude approximations.
- ⁴⁵R. Alben, D. Weaire, J. E. Smith, Jr., and M. H. Brodsky, *Phys. Rev. B* **11**, 2271 (1975).
- ⁴⁶M. V. Vol'kenshtein, *C. R. Acad. Sci. USSR* **32**, 185 (1941).
- ⁴⁷G. W. Chantry, in *The Raman Effect*, edited by A. Anderson (Dekker, New York, 1971), Vol. 1, Chap. 2, pp. 74-85.
- ⁴⁸D. A. Long, *Proc. R. Soc. London A* **217**, 203 (1953).
- ⁴⁹R. Tubino and L. Piseri, *Phys. Rev. B* **11**, 5145 (1975).
- ⁵⁰R. Loudon, *Adv. Phys.* **13**, 423 (1964).
- ⁵¹A. A. Maradudin, E. W. Montroll, and G. H. Weiss, "Theory of Lattice Dynamics in the Harmonic Approximation," Supplement 3 to *Solid State Physics* (Academic Press, 1963); 2nd ed. with I. P. Ipatova as additional author (1971).
- ⁵²W. H. Press, B. P. Flannery, S. A. Teukolsky, and W. T. Vetterling, *Numerical Recipes* (Cambridge University Press, New York, 1986), Sec. 11.4.
- ⁵³J. C. Decius and R. M. Hexter, *Molecular Vibrations in Crystals* (McGraw Hill, New York, 1977).
- ⁵⁴J. H. Gieske, T. Aselage, and D. Emin, in *Boron-Rich Solids, 1990* (Ref. 1a).
- ⁵⁵W. A. Harrison, *Electronic Structure and the Properties of Solids* (Dover, New York, 1989), Chaps. 8 and 9.
- ⁵⁶F. H. Horn, *J. Appl. Phys.* **30**, 1611 (1959).
- ⁵⁷*Boron Hydride Chemistry*, edited by E. L. Muetterties (Academic, New York, 1975).
- ⁵⁸J. A. Koningstein and O. S. Mortensen, in *The Raman Effect*, edited by A. Anderson (Dekker, New York, 1973), Vol. 2, Chap. 8.
- ⁵⁹M. V. Klein, in *Topics in Applied Physics, Light Scattering in Solids I*, edited by M. Cardona (Springer-Verlag, New York 1983).
- ⁶⁰In 1957, prior to the credited discovery of the α form (Ref. 25), Shaw, Hudson, and Danielson [*Phys. Rev.* **107**, 419 (1957)] determined electrical properties of boron crystals. Some "special crystals" had very low room-temperature resistivities and an activation energy as low as 0.06 eV. This was attributed by Shaw, Hudson, and Danielson to donor impurity levels. Horn (Ref. 56) however, speculated on whether the special crystals were simple rhombohedral boron which nowadays we call α -boron.